Upper-Ocean Eddy Heat Flux across the Antarctic Circumpolar Current in Drake Passage from Observations: Time-Mean and Seasonal Variability

MANUEL O. GUTIERREZ-VILLANUEVA, TERESA K. CHERESKIN, AND JANET SPRINTALL

Scripps Institution of Oceanography, University of California, San Diego, La Jolla, California

(Manuscript received 5 November 2019, in final form 23 May 2020)

ABSTRACT

Eddy heat flux plays a fundamental role in the Southern Ocean meridional overturning circulation, providing the only mechanism for poleward heat transport above the topography and below the Ekman layer at the latitudes of Drake Passage. Models and observations identify Drake Passage as one of a handful of hot spots in the Southern Ocean where eddy heat transport across the Antarctic Circumpolar Current (ACC) is enhanced. Quantifying this transport, however, together with its spatial distribution and temporal variability, remains an open question. This study quantifies eddy heat flux as a function of ACC streamlines using a unique 20-yr time series of upper-ocean temperature and velocity transects with unprecedented horizontal resolution. Eddy heat flux is calculated using both time-mean and time-varying streamlines to isolate the dynamically important across-ACC heat flux component. The time-varying streamlines provide the best estimate of the across-ACC component because they track the shifting and meandering of the ACC fronts. The depth-integrated (0–900 m) across-stream eddy heat flux is maximum poleward in the south flank of the Subantarctic Front (-0.10 ± 0.05 GW m^{-1}) and decreases toward the south, becoming statistically insignificant in the Polar Front, indicating heat convergence south of the Subantarctic Front. The time series provides an uncommon opportunity to explore the seasonal cycle of eddy heat flux. Poleward eddy heat flux in the Polar Front Zone is enhanced during austral autumn–winter, suggesting a seasonal variation in eddy-driven upwelling and thus the meridional overturning circulation.

1. Introduction

The Southern Ocean meridional overturning circulation plays a fundamental role in the global climate and transfers heat, salt, and biochemical tracers across the eastward-flowing Antarctic Circumpolar Current (ACC). Meridional transport in the Southern Ocean requires crossing the intense zonal ACC jets that represent strong physical barriers for the cross-frontal exchange of particles or tracers. Eddies break these barriers by flattening the isopycnals and weakening the potential vorticity gradients, allowing particles to cross the fronts. In particular, eddy-driven heat transport provides the sole mechanism for poleward heat transport at depths above submerged topography at the latitudes of Drake Passage (e.g., Meredith et al. 2011, and references therein). This poleward heat transport balances the surface northward Ekman heat transport and air–sea heat fluxes. Quantifying the amount of heat transferred poleward by eddies, therefore, is crucial for understanding the Southern Ocean heat budget.

Although the classical zonally averaged theory has provided many insights into ACC dynamics (Marshall and Radko 2003), the Southern Ocean and the ACC are highly heterogeneous. Satellite altimetry, numerical models, and the global array of Argo floats reveal that the distribution of eddy activity is concentrated in a handful of eddy hot spots downstream of abrupt bottom topography and in western boundary currents (e.g., Abernathey and Cessi 2014; Thompson and Naveira Garabato 2014; Chapman and Sallée 2017; Foppert et al. 2017). Direct eddy heat flux estimates in these hot spots (Bryden 1979; Nowlin et al. 1985; Phillips and Rintoul 2000; Walkden et al. 2008; Ferrari et al. 2014; Lenn et al. 2011; Watts et al. 2016), enable understanding of the contribution of the eddies to the meridional overturning circulation but leave open the question of how representative these estimates are for the Southern Ocean. Neutrally buoyant floats (Gille 2003) and Argo floats (Chapman and Sallée 2017) have provided global eddy heat flux estimates in the Southern Ocean, but the coarse

Corresponding author: Manuel O. Gutierrez-Villanueva, mog002@ucsd.edu

DOI: 10.1175/JPO-D-19-0266.1

temporal and spatial sampling smooths the spatial distribution and reduces the magnitude of these heat flux estimates. Overall, quantifying the amount of heat transported by eddies across the ACC requires densely sampled and simultaneous velocity and temperature observations to obtain statistically significant estimates, which remains a challenge as these types of observations in the Southern Ocean are scarce.

A problematic aspect of the eddy heat flux calculation is that net flux results only from the horizontally divergent component. As discussed by Marshall and Shutts (1981), the eddy heat flux vector can be decomposed into the sum of two components: a rotational component that circulates around eddy potential energy contours and a divergent component that represents the dynamically important net downgradient heat flux. Neglecting the distinction between rotational and divergent components can erroneously indicate a higher rate of baroclinic conversion of potential to kinetic energy than is present. Nevertheless, reducing the rotational component from observations remains nontrivial. Several authors have used different methods to calculate the divergent component. For instance, Lenn et al. (2011) used a time-mean streamwise coordinate system to estimate the across-stream eddy heat flux component from 7 years of along-track temperature and current velocity observations in Drake Passage. Phillips and Rintoul (2000) used daily shear coordinates to isolate the across-stream component from an array of four current meter moorings deployed for 2 years south of Tasmania. Following Marshall and Shutts (1981), Cronin and Watts (1996) estimated the divergent component in the Gulf Stream as the residual of the eddy heat flux vector projected along temperature variance contours minus the total eddy heat flux vector. Bishop et al. (2013) showed that the barotropic (depth independent; in this case, near-bottom current) component naturally captures the full divergent component with a small rotational residual in the Kuroshio Extension. Watts et al. (2016) applied this technique in Drake Passage; they concluded that baroclinic instabilities were the leading mechanism for the large heat flux events that occurred when the barotropic component crossed the baroclinic component at an angle resulting in a deviation from the vertically aligned equivalent barotropic flow. Their 4-yr time series captured these short 4–6-day events and produced stable estimates over 2-yr subsets. However, their results have a spatial resolution of 40–60 km, coarser than the first baroclinic Rossby radius (20–10 km) at that latitude range (Chelton et al. 1998). Foppert et al. (2017) used 23 years of altimetric sea surface height (SSH) variance as a proxy for downgradient eddy heat flux, but again the SSH maps have coarse spatial resolution [O(100 km)].

Mesoscale eddies contribute to the stratification and ventilation of the thermocline in the Southern Ocean. However, the magnitude of their contribution to the seasonal variation of the upper-ocean heat content is not well understood. Recent studies in Drake Passage from observations showed that half of the variance of the seasonal upper-ocean heat content is explained by the air–sea heat fluxes (Stephenson et al. 2012) which, combined with the eddy advection and interannual variability, accounted for ~84% of the variance (Stephenson et al. 2013). Since the air–sea heat fluxes account for most of the seasonal variability of the upper-ocean heat content in Drake Passage, the implication is that the contribution of mesoscale eddies plays a minimal role. However, air–sea flux products are poorly constrained in the Southern Ocean because of the severe undersampling relative to other regions of the world's oceans. Also, eddy heat diffusion and advection processes could potentially play an important role in the Southern Ocean eddy hot spots. The lack of long-term observations in these regions impedes us from understanding the potential role of eddies in the seasonal variations of the upper-ocean heat budget.

Drake Passage is a known hot spot of eddy activity (e.g., Thompson and Sallée 2012; Thompson and Naveira Garabato 2014). In this study, we use a unique 20-yr time series of nearly repeated upper-ocean temperature and velocity transects in Drake Passage with an unprecedented spatial resolution of the order of the first baroclinic Rossby radius. These observations provide an opportunity to characterize both the mean and eddy temperature and velocity fields with statistical significance. The eddy heat flux across the ACC within Drake Passage is estimated relative to the position of the major ACC fronts. Lenn et al. (2011) previously calculated the time-mean eddy heat flux using the Drake Passage temperature and velocity transects over the upper 250-m range of depth for the period from September 1999 to October 2006. In this paper, we extend the Lenn et al. (2011) estimates both in depth (to 900 m) and in time (from September 1999 to December 2014). Furthermore, in addition to a time-mean streamwise coordinate system (Lenn et al. 2011), we also adopt a time-varying, synoptic streamwise coordinate system to decompose the eddy heat flux vector into the rotational along-stream component and the divergent across-stream component; it is the divergent component that represents the true net heat flux across the ACC. The synoptic coordinate system combined with the high spatial resolution of the Drake Passage transects allows the study of the effect of the shifting and meandering of the ACC fronts on the cross-frontal eddy heat flux. Last, the 20-yr time series uniquely enables us to estimate the mean eddy kinetic energy (EKE) and to explore the seasonality of the

eddy heat flux and EKE relative to the position of the ACC fronts.

Our results focus on the across-stream eddy heat flux that gives rise to a local net poleward heat transport from eddies. We also present the along-stream eddy heat flux to gauge its magnitude in comparison to the across-stream component. The along-stream component is thought to be dynamically unimportant because it recirculates heat along the re-entrant path of the ACC. This path is not purely zonal, however; the ACC traverses hundreds of kilometers meridionally as it travels from its southernmost point at about 65°S in the southeastern Pacific Ocean to its northernmost point at about 45°S in the Brazil–Malvinas Confluence. The ACC temperature changes along this path, with warming across the confluence and along the Agulhas Extension and cooling along the high-latitude Pacific segment; consequently warm and cold waters respectively advect poleward and equatorward, with negligible meridional mass transport, resulting in a net poleward heat transport (Sun and Watts 2002). Air–sea interaction and mesoscale eddies play essential roles in changing the along-path ACC temperature. The along-stream eddy heat flux contributes to this larger-scale ACC heat transport.

The paper is structured as follows: Section 2 provides details of the Drake Passage time series and remotely sensed datasets. Methods to obtain the time-mean geostrophic velocities and streamlines and temperature fields are discussed in section 3. Also in this section, the binning, rotation, and averaging of the eddy heat flux components are described for each streamwise coordinate system. Section 4 describes the mean temperature and geostrophic streamline fields. The eddy heat flux estimates using both the time-mean and synoptic streamlines are presented in section 5. This section also describes the seasonal cycle of the near-surface eddy heat flux components and EKE using the synoptic streamlines. Section 6 discusses the results and compares these with earlier eddy heat flux studies that have attempted to estimate the divergent component from observations. Last, section 7 presents the summary and conclusions.

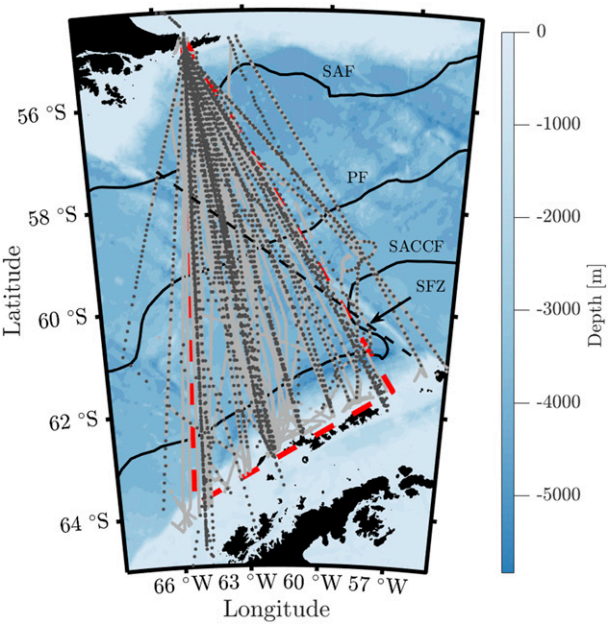

FIG. 1. Map showing the *LMG* transects in Drake Passage with bathymetry from Smith and Sandwell (1997). Dark- and light-gray lines show the XBT and underway ADCP velocity transects, respectively. Red dashed lines show the area enclosed by the most repeated transects. Solid black lines show the location of the major ACC fronts (Orsi et al. 1995): the Subantarctic Front (SAF), Polar Front (PF), and Southern ACC Front (SACCF). The dashed black line marks the axis of the Shackleton Fracture Zone (SFZ).

2. Datasets

a. The Drake Passage observations

Underway upper-ocean velocity and temperature were collected aboard the Antarctic Research and Supply Vessel (ARSV) *Laurence M. Gould* (*LMG*) that transits between South America and the Antarctic Peninsula (Fig. 1). Details of the different datasets can be found in Table 1. In this study, we use the 150-kHz acoustic Doppler current profiler (ADCP; NB150) time series that has been described by Lenn et al. (2007). In summary, starting in September 1999 the NB150 time series provides velocity measurements in the upper 300 m at 8-m vertical resolution. In addition, since November 2004 a 38-kHz ADCP (OS38) started sampling velocity at a vertical resolution of 24 m extending to 1222-m depth. Here we use only the upper 900 and 250 m since the velocity profiles are gappier below this depth for the OS38 and NB150 ADCP, respectively; also, the temperature data only spans the upper 890 m (described below). From September 1999 to December 2014, 326 NB150 and 204 OS38 ADCP transects are available (Table 1). In contrast, Lenn et al. (2011) used 156 NB150 velocity transects.

Velocity data were processed using the Common Ocean Data Access System (CODAS) software (Firing et al. 2012); velocities were transformed from ship-relative to absolute ocean currents using the GPS position and attitude measurements. Because the sonar wells are filled with an antifreeze mixture, a speed of sound correction is made using measured sound velocity from a probe mounted in the NB150 well. The OS38 uses a phased array transducer that does not require a sound speed correction. The OS38 does, however, require an

TABLE 1. The Drake Passage datasets.

Instrument	XBT	NB150 ADCP (150 kHz)	OS38 ADCP (38 kHz)
Depth range (m)	0–900	24–320	42–1222
Max depth used (m)	890	250	900
Gridded depth resolution (m)	10	8	24
Along-track resolution (km)	6–10[a]; 10–15[b]	5	5
Sampling period	Sep 1996–Dec 2016	Sep 1999–Dec 2014	Nov 2004–Dec 2014
No. of cruises	130	326	204
XBT–ADCP paired transects	—	108	63

[a] Across the Subantarctic Front and Polar Front.
[b] Elsewhere in Drake Passage.

additional correction to account for residual ADCP transducer misalignment that we estimated from minimizing transport bias as in Firing et al. (2011). The absolute velocity is averaged over 300 s corresponding to ~5-km along-track horizontal resolution. Barotropic tidal currents were removed from the absolute velocity by subtracting the tidal prediction of the TOPEX/Poseidon 7.2 (TPXO7.2) tide model (Egbert et al. 1994). Baroclinic tides and ageostrophic Ekman currents were not removed from the velocity data because they have relatively small amplitudes [$<O(10)\,\mathrm{cm\,s^{-1}}$] in Drake Passage (Lenn et al. 2007; Lenn and Chereskin 2009); moreover, it is impractical to remove these flows within uncertainty for each transect.

On 6–7 *LMG* transects per year, 70 expendable bathythermograph (XBT) probes were deployed that measure temperature in the upper 900 m (Table 1). The temperature profiles were averaged to bins of 10 m in depth. The spatial resolution is 6–10 km across the Subantarctic Front (SAF) and Polar Front (PF) and 10–15 km elsewhere (Sprintall 2003). All data were quality controlled, and, following the method of Hanawa et al. (1995), the XBT data were corrected for the systematic fall-rate error. Overall, there are 130 XBT transects from September 1996 to December 2016 that were used to calculate the time-mean temperature fields; 63 of these surveys coincide with the OS38 ADCP transects from November 2004 to December 2014, and 108 coincide with the NB150 from September 1999 to December 2014. Lenn et al. (2011) used 38 concurrent XBT and NB150 velocity transects between September 1999 and October 2004.

b. *Remotely sensed data*

In this study we estimate the time-mean geostrophic streamfunction $\overline{\Psi}$ and the synoptic coordinate system Ψ^* using the SSALTO/DUACS daily maps of SSH anomaly, objectively mapped from multiple satellite altimeters to a 0.25° × 0.25° Cartesian grid, produced and distributed by the Copernicus Marine and Environmental Monitoring Service (CMEMS; Ducet et al. 2000). The SSH anomalies are relative to a 20-yr mean of the SSH field. We only consider the SSH anomalies from September 1999 to December 2014, which covers our period of interest. We also use the mean dynamic topography from Maximenko et al. (2009) derived from a combination of 20 years of satellite altimetry, gravity measurements, and in situ data.

3. Methods

a. *Estimating mean temperature and geostrophic velocity and streamfunction*

The geographic coordinate system was rotated 24° counterclockwise to establish an along/across Drake Passage coordinate system. The area enclosed by the most repeated transects (Fig. 1) was gridded into horizontal boxes with a 25 km × 25 km resolution as in Lenn et al. (2011) and Firing et al. (2011). The grid was employed for calculating the mean velocity and temperature fields at each depth bin.

For the mean velocity, the surface geostrophic velocity anomalies calculated from the daily SSH maps were subtracted from the ADCP velocities at each depth to reduce the eddy aliasing (Lenn et al. 2008; Firing et al. 2011). The ADCP velocities from each transect were then averaged within the Drake Passage grid to produce one velocity profile per occupied grid box per transect. The velocity profiles in each grid were then averaged over all cruises to produce a record-length mean velocity profile per grid box. In the upper 24 or 42 m where the NB150 or OS38 ADCP, respectively, did not sample, a slab layer was assumed.

To calculate the Drake Passage mean geostrophic streamfunction $\overline{\Psi}$ and velocities $\overline{\mathbf{u}}$, we followed Firing et al. (2011) and Lenn et al. (2008). The objective mapping constrained the mean velocity profiles and streamfunction to satisfy the geostrophic continuity relationship (i.e., $\nabla_h \cdot f\mathbf{U} = 0$, where f is the Coriolis parameter and $\mathbf{U}$ is the total velocity vector). First, the background-mean geostrophic velocities were calculated by taking spatial

gradients from the Maximenko et al. (2009) mean dynamic topography and removing them from the mean velocity profiles. The anomalies were objectively mapped assuming a Gaussian covariance function and an isotropic decorrelation scale of 70 km (Lenn et al. 2008; Firing et al. 2014) and a noise-to-signal ratio of 0.2. The decorrelation scales were varied by ±15 km, and the noise-to-signal ratio was varied by ±0.1, but the mapped geostrophic streamlines and velocities were not sensitive to these changes. A smaller decorrelation scale potentially affects the mapping error in the southern Drake Passage area ($y < -500$ km) where gaps between transects widen in the down-passage (x axis) orientation. The mean dynamic topography from Rio and Hernandez (2004) was also tested, but the mapped mean streamfunction and velocities were insensitive to the choice of the background mean, as also noted by Firing et al. (2011). The mean geostrophic streamfunction and velocities from the Maximenko et al. (2009) dynamic topography were added back to the mapped geostrophic streamfunction and velocity anomalies.

The same 25 km × 25 km grid boxes along/across Drake Passage used to construct the mean ADCP profiles were also used to calculate the mean temperature fields $\overline{T}$. All 130 XBT transects from September 1996 to December 2016 were used to construct the mean. Temperature profiles were first linearly interpolated to the same ADCP depth bins and for each grid box were averaged by transect and then over the complete time period.

b. Estimating streamwise-averaged eddy heat flux

Temperature fluctuations T' were calculated at the location of each temperature profile T by removing the gridded time-mean temperature estimated for the grid box that contains the individual temperature profile: $T'(x, y, z, t) = T(x, y, z, t) - \overline{T}(x_g, y_g, z)$, where (x_g, y_g) correspond to the temperature profile's 25 km × 25 km grid box. Similarly, velocity fluctuations $\mathbf{u}'$ were obtained by removing their corresponding objectively mapped time-mean geostrophic velocity vector $\overline{\mathbf{u}}$ from the instantaneous velocity vector $\mathbf{u}$ profile $\mathbf{u}'(x, y, z, t) = \mathbf{u}(x, y, z, t) - \overline{\mathbf{u}}(x_g, y_g, z)$.

Using the Drake Passage transect data, it is infeasible to decompose the eddy heat flux vector $\mathbf{u}'T'$ into rotational and divergent components following the method of Marshall and Shutts (1981). Instead, we use streamwise components for the heat flux decomposition. In a truly instantaneous streamwise coordinate system, the along-stream $u'T'_\Psi$ contains all of the rotational component while the across-stream $v'T'_\Psi$ contains all of the divergent component; that is, $v'T'_\Psi$ represents the net eddy heat flux across the ACC. However, the synoptic streamlines that we use are approximations to the true instantaneous streamlines at the time and location of the observations. We assume that the across-stream eddy heat flux component contains most of the divergent eddy heat flux plus some rotational residual. Likewise, the along-stream component contains most of the rotational eddy heat flux plus some divergent residual.

1) Time-mean streamwise coordinate system $\overline{\Psi}$

To obtain the streamwise-averaged eddy heat flux components using the time-mean coordinate system, we contoured $\overline{\Psi}$ at every depth with a streamline spacing of $\Delta\overline{\Psi} = 0.05$ m; the streamlines were selected between the maximum and minimum $\overline{\Psi}$ values (−0.575 and −1.625 m, respectively) that can be mapped at the deepest bin (886 m) and are delimited by the 500-m isobath in the direction across Drake Passage (Fig. 2). Next, the individual velocity and temperature data positions that fell within a specific pair of streamlines $\overline{\Psi}_j$ and $\overline{\Psi}_{j+1}$ were determined for all transects, where $j = 1, 2, \ldots, M - 1$ (M is the total number of open streamlines; $\overline{\Psi}_{j=1}$ is the northernmost streamline, and $\overline{\Psi}_{j+1} = \overline{\Psi}_j - \Delta\overline{\Psi}$). Subsequently, for each individual temperature data location, the closest individual velocity data position was determined and the eddy heat flux vector was calculated and assigned to the temperature data position. The normal vector $\hat{\mathbf{n}} = \nabla\overline{\Psi}/|\nabla\overline{\Psi}|$ was bilinearly interpolated to the individual heat flux positions, and the eddy heat flux vector was rotated to an angle $\theta = \theta_{\hat{\mathbf{n}}} - \pi/2$, where $\theta_{\hat{\mathbf{n}}}$ represents the angle of the normal vector measured from the $+x$ axis. With this rotation, the along-stream and across-stream components are $u'T'_{\overline{\Psi}}$ and $v'T'_{\overline{\Psi}}$, respectively. Components were streamwise averaged at each depth per streamline for each transect. To obtain mean eddy heat flux estimates ($\overline{u'T'_{\overline{\Psi}}}$, $\overline{v'T'_{\overline{\Psi}}}$), each component per transect per streamline was averaged by combining all of the available Drake Passage transects. The standard errors $\hat{\sigma}$ were calculated for each eddy heat flux component as $\hat{\sigma} = \sigma/\sqrt{N}$, where σ and N are the standard deviations of each component and the number of degrees of freedom, respectively. Each concurrent temperature and velocity transect was assumed to represent one degree of freedom (Lenn et al. 2011).

2) Time-varying streamwise coordinate system Ψ^*

To estimate the effect of the temporal shifting of the ACC geostrophic streamlines in the eddy heat flux calculation (Fig. 2), a time-varying streamwise coordinate system Ψ^* was adopted; Ψ^* allowed us to track both the position of the ACC fronts and the orientation of the flow. We expanded the domain beyond that of $\overline{\Psi}$ and

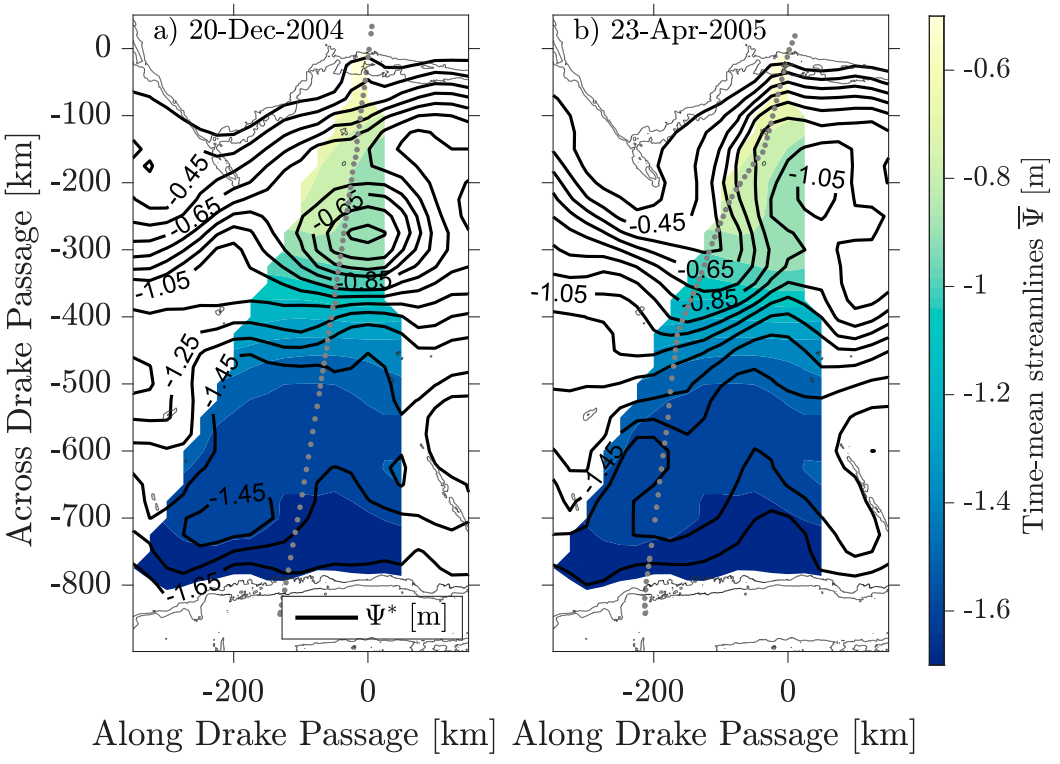

FIG. 2. Maps of time-mean $\overline{\Psi}$ (color bar) and time-varying Ψ^* (black solid lines) geostrophic streamfunction for (a) 20 Dec 2004 and (b) 23 Apr 2005. Streamlines are contoured at 0.10-m intervals. XBT profile positions (gray dots) and 500 and 1000-m isobaths (thin gray lines) are indicated.

$\overline{T}$ (area enclosed by most repeated transects; filled contours in Fig. 2). The expanded domain allowed us to distinguish open streamlines from closed contours that might represent eddies (solid contours; Fig. 2). The synoptic streamlines were calculated as $\Psi^* = \overline{\Psi}^0_{-250} + \Psi^{\text{ssh}}$, where Ψ^{ssh} is an SSH anomaly map averaged over a 5-day window centered at the mean date of each transect and $\overline{\Psi}^0_{-250} = 1/250 \int^0_{-250} \overline{\Psi}\, dz$ is the objectively mapped mean streamfunction depth-averaged over the upper 250 m. We chose $\overline{\Psi}^0_{-250}$ since there is little vertical depth variation in the ACC in Drake Passage in the upper 250 m; moreover, $\overline{\Psi}^0_{-250}$ is consistent with the depth range of the temperature definitions for the ACC fronts (Orsi et al. 1995; Sprintall 2003). Away from the area enclosed by the most repeated transects, the Maximenko et al. (2009) mean dynamic topography was used for the time-mean streamlines (Fig. 2). The streamlines $-0.35 \le \Psi^* \le -1.65$ m were mapped at $\Delta\Psi^* = 0.10$ m. A larger contour spacing was used than that adopted for the time-mean streamlines since the spacing between synoptic streamlines is smaller compared to that of $\overline{\Psi}$ (Fig. 2). This reduced the resolution by half but allowed at least one data point per pair of streamlines per transect.

The synoptic streamlines show high mesoscale activity including cold and warm core rings detaching from the ACC fronts and strong meandering of the fronts (Fig. 2). Data points that fall inside closed contours (rings) represent a challenge as to how to assign and bin them into a unique contour interval. Since 31 of 63 transects from November 2004 to December 2014 sampled within rings or meanders, it is desirable to devise a consistent method for the streamwise binning, rotation and averaging of each eddy heat flux component.

Three methods were tested for the rotation, binning and averaging. Method 1 looks for velocity and temperature data falling within open streamlines, whereas methods 2 and 3 find data falling inside unique intersections between each transect and open streamlines moving in the down-along-transect or up-along-transect direction, respectively. Unique intersections were defined where each transect first intersects an open streamline moving in the along-transect direction; multiple intersections for a transect (i.e., crossing a specific contour more than once) were not allowed. We then calculated individual eddy heat flux vectors and rotated them into along-stream and across-stream components as in the time-mean streamlines, except when data points fell inside closed contours (method 1) or/and cross through strong meandering (method 2 or 3). In those cases, the normal vector was reinterpolated

using an inverse distance weighting method using neighboring data points. Subsequently, the eddy heat flux vector was rotated using the reinterpolated normal vector angle, and binned and averaged per pair of streamlines.

Appendix A expands the steps followed in each method. Eddy heat flux estimates determined from each method are mostly sensitive in the northern half of Drake Passage ($-0.50 > \overline{\Psi} > -1.10$ m). In the following, only results using method 1 are shown because methods 2 and 3 show a similar spatial distribution of the eddy heat flux components. Appendix B presents the depth-integrated components calculated using methods 2 and 3.

4. Mean fields of geostrophic streamfunction $\overline{\Psi}$ and temperature $\overline{T}$

Maps of the objectively mapped streamfunction $\overline{\Psi}$ for two different depths (70 and 838 m) are shown in Figs. 3a and 3b. The instantaneous positions of the three major ACC fronts were determined using subsurface temperature criteria (Orsi et al. 1995; Sprintall 2003) calculated from the temperature transects (Lenn et al. 2011); these criteria identify the main fronts uniquely and do not distinguish potential multiple jets associated with each front (e.g., Sokolov and Rintoul 2009). Consequently, we determined the range of streamlines associated with each front as the streamline values that fell between the 25th and 75th percentiles of the instantaneous positions of each front; the streamlines marking the energetic Polar Front Zone (PFZ) that lies between the SAF and PF are also given (Table 2). The SAF shows large meandering throughout the upper 900 m. The SAF has a northeast orientation following the bathymetry, whereas the PF is quasi aligned with the down-passage direction; its streamlines show convergence at $-100 \leq x \leq 0$ km, implying that the PF mean velocity slightly increases (Figs. 3a,b). The three-dimensional structure of the time-mean ACC in Drake Passage is consistent with the equivalent barotropic structure of the ACC; that is, streamlines are self-similar with depth, as also found by Lenn et al. (2008) and Firing et al. (2011). The region between the PF and the Southern ACC Front (SACCF) is relatively quiescent, as the spacing between contours is the largest in the Drake Passage data fan. The maps of geostrophic streamlines are within the prescribed noise-to-signal ratio (red line in Figs. 3a,b). Firing et al. (2011) calculated mean maps of geostrophic velocities and streamfunction using 105 OS38 velocity transects, that is, one-half of the number of transects used in our work. However, their maps have gaps south of the PF as their mapping error was larger than their prescribed noise. By increasing the number of OS38 velocities transects by twofold over those employed by Firing et al. (2011), we resolved the mean ACC structure in Drake Passage at each depth bin in the area enclosed by the most repeated transects (Fig. 1) and within the noise-to-signal ratio (Figs. 3a,b).

The mean temperature fields $\overline{T}$ at two different depths (70 and 838 m; Figs. 3c,d) show maximum temperatures located near the South American continental slope: Subantarctic Surface Water in the upper layer and Subantarctic Mode Water below. The 2° isotherm is located between $-400 \leq y \leq -350$ km, corresponding to the mean position of the PF (Sprintall 2003). The position of the PF delimits the area where the Antarctic Surface Water (AASW) mass subducts and flows north underneath the Subantarctic Water (Orsi et al. 1995). South of the PF, AASW is present as a subzero surface layer extending to 150 m (Sprintall 2003). Below the AASW, Upper Circumpolar Deep Water is found, and it is characterized by temperatures around 1.8°C (Orsi et al. 1995).

5. Eddy heat flux estimates

This section presents the mean along/across stream eddy heat flux components and mean depth-integrated eddy heat flux components and their respective standard errors using the 1) time-mean $\overline{\Psi}$ and 2) synoptic Ψ^* streamwise coordinate system (method 1: area between a pair of streamlines). The mean eddy heat flux estimates ($\overline{\mathbf{u}'T'_{\overline{\Psi}}}$ and $\overline{\mathbf{u}'T'_{\Psi^*}}$) and standard errors ($\hat{\sigma}_{\overline{\mathbf{u}'T'_{\overline{\Psi}}}}$ and $\hat{\sigma}_{\overline{\mathbf{u}'T'_{\Psi^*}}}$) as a function of depth and streamline are given in degrees Celsius meters per second. The mean eddy heat flux estimates are equivalent to the average flux per area in kilowatts per meter squared when multiplied by ρC_p, where $\rho = 1030\,\mathrm{kg\,m^{-3}}$ and $C_p = 4000\,\mathrm{J\,kg^{-1}\,K^{-1}}$ are the seawater density and specific heat capacity, respectively. Depth-integrated estimates ($\rho C_p \int_{-H}^{0} \overline{\mathbf{u}'T'_{\overline{\Psi}}}\, dz$ and $\rho C_p \int_{-H}^{0} \overline{\mathbf{u}'T'_{\Psi^*}}\, dz$) are given in gigawatts per meter, which represents the average heat flux per ACC unit length in the upper 886 m. A positive along-stream and across-stream flux indicates downstream and equatorward eddy heat flux, respectively. Only statistically significant estimates per area are shown.

a. *Time-mean streamwise coordinate system* $\overline{\Psi}$

The along-stream component $\overline{u'T'_{\overline{\Psi}}}$ (Fig. 4a) has the largest downstream heat flux in the northern flank of the PF ($-0.90 \geq \overline{\Psi} \geq -1.00$ m; $0.14°\mathrm{C\,m\,s^{-1}}$) with a second peak south of the PF ($-1.25 \geq \overline{\Psi} \geq -1.35$ m) of $0.07°\mathrm{C\,m\,s^{-1}}$. Both peaks are maximum in the upper 200 m and then

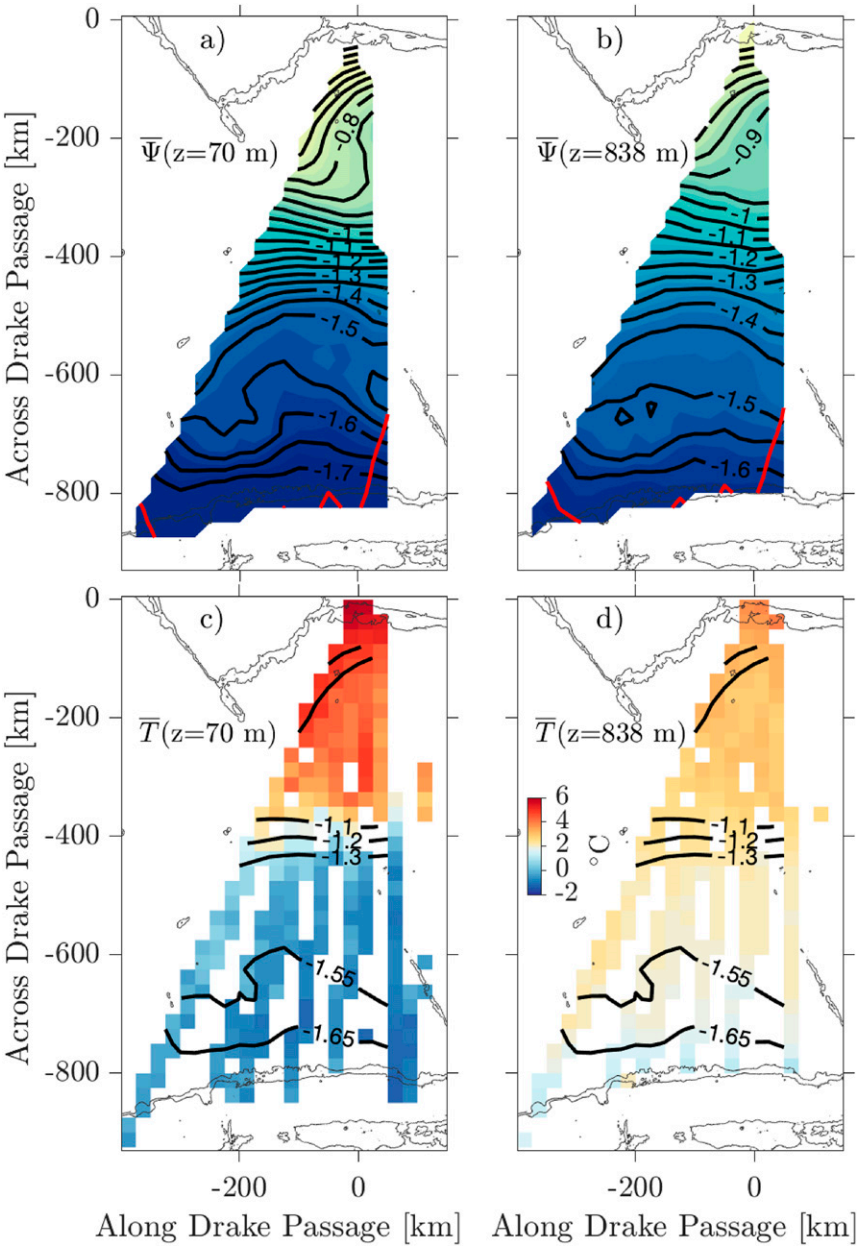

FIG. 3. (a),(b) Mean geostrophic streamfunction $\overline{\Psi}$ and (c),(d) temperature $\overline{T}$ fields calculated from the *LMG* observations at (left) 70 and (right) 838 m. Streamfunction in (a) and (b) is contoured at $\Delta\Psi = 0.05$ m within the area enclosed by the most repeated transects (Fig. 1). The red solid line shows the mapping error $E = 0.20$. The x and y axis are kilometers along and across passage, respectively. Missing data are the blank grid boxes. The 500- and 1000-m isobaths are contoured (light gray). The black solid contours in (c) and (d) correspond to the time-mean streamline boundaries of each ACC front averaged between 200- and 300-m depth (see Table 2).

decrease below. The SAF and the PFZ ($\overline{\Psi} > -0.80$ m) in general show upstream heat flux peaking near the surface (from $-0.07°$ to $-1.00°$C m s^{-1}); south of the PF, the along-stream component also shows upstream heat flux but only in the upper 180 m and changes below to downstream eddy heat flux. The across-stream component $\overline{v'T'_{\Psi}}$ is poleward in the SAF and PFZ throughout the sampled water column (Fig. 4b). The largest poleward heat flux in Drake Passage is found on the northern flank of the PF and in the southern

TABLE 2. Mean streamfunction $\overline{\Psi}$ intervals and latitude range for the ACC fronts. Both streamfunction and latitude values correspond to the values that fall between the 25th and 75th percentiles of the instantaneous positions of each front. Streamfunction values of each front are relative to the mean streamfunction $\overline{\Psi}$ averaged between 200- and 300-m depth.

	SAF	PFZ	PF	SACCF
$\overline{\Psi}$ (m)	$-0.50 \geq \overline{\Psi} \geq -0.70$	$-0.70 > \overline{\Psi} > -1.10$	$-1.10 \geq \overline{\Psi} \geq -1.30$	$-1.55 \geq \overline{\Psi} \geq -1.65$
Lat range	$-55.54° \geq$ lat $\geq -56.15°$	$-56.15° \geq$ lat $\geq -58.01°$	$-58.01° \geq$ lat $\geq -58.90°$	$-61.04° \geq$ lat $\geq -62.45°$

half of the PFZ, with a peak value of $-0.17°\text{C m s}^{-1}$ in the upper 150 m and decreases with depth. In addition, poleward flux (from $-0.08°$ to $-0.03°\text{C m s}^{-1}$) is found within the PF ($-1.15 \geq \overline{\Psi} \geq -1.25$ m) from 100- to 350-m depth. The SAF shows significant poleward flux (from $-0.05°$ to $-0.02°\text{C m s}^{-1}$) throughout the sampled water column. The standard errors of each component ($\hat{\sigma}_{\overline{u'T'}_{\overline{\Psi}}}$, $\hat{\sigma}_{\overline{v'T'}_{\overline{\Psi}}}$) are high ($>0.02°\text{C m s}^{-1}$) from the surface down to 400-m depth between the SAF and the PF and shoaling poleward (Figs. 4c,d). The marginal to insignificant eddy heat flux and the smaller errors south of the PF suggest that there is less eddy activity in this area relative to within the main fronts farther north. The along-stream standard error $\hat{\sigma}_{\overline{u'T'}_{\overline{\Psi}}}$ is largest near the surface on the southern flank of the PF (Fig. 4c). On the other hand, the across-stream standard error $\hat{\sigma}_{\overline{v'T'}_{\overline{\Psi}}}$ has a surface maximum ($>0.05°\text{C m s}^{-1}$) in the south flank of the PFZ (Fig. 4d) that is collocated with the maximum poleward heat flux in the ACC (Fig. 4b).

b. *Synoptic streamwise coordinate system* Ψ^*

In this section, mean eddy heat flux components and their respective standard errors for the synoptic streamlines Ψ^* employing method 1 (see appendix A) are shown. The along-stream component $\overline{u'T'}_{\Psi^*}$ is significant

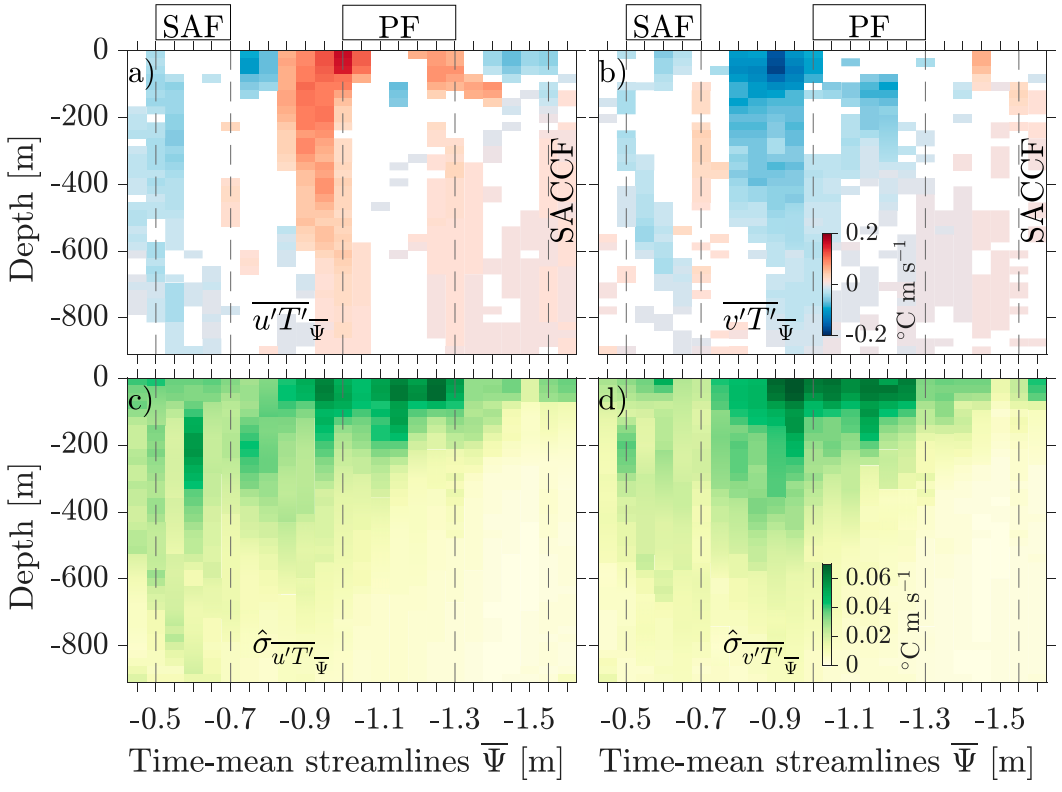

FIG. 4. (a) Along-stream $\overline{u'T'}_{\overline{\Psi}}$ and (b) across-stream $\overline{v'T'}_{\overline{\Psi}}$ eddy heat flux components calculated in a time-mean streamwise coordinate system $\overline{\Psi}$. Positive along-stream and across-stream values indicate downstream and equatorward heat flux, respectively. Only statistically significant eddy heat flux estimates are shown. (c) Along-stream $\hat{\sigma}_{\overline{u'T'}_{\overline{\Psi}}}$ and (d) across-stream $\hat{\sigma}_{\overline{v'T'}_{\overline{\Psi}}}$ standard errors. Eddy heat flux components and their standard errors are plotted at $\Delta\overline{\Psi} = 0.05$ m. Streamfunction values for the ACC fronts are shown in dashed lines (Table 2). Streamfunction decreases moving poleward.

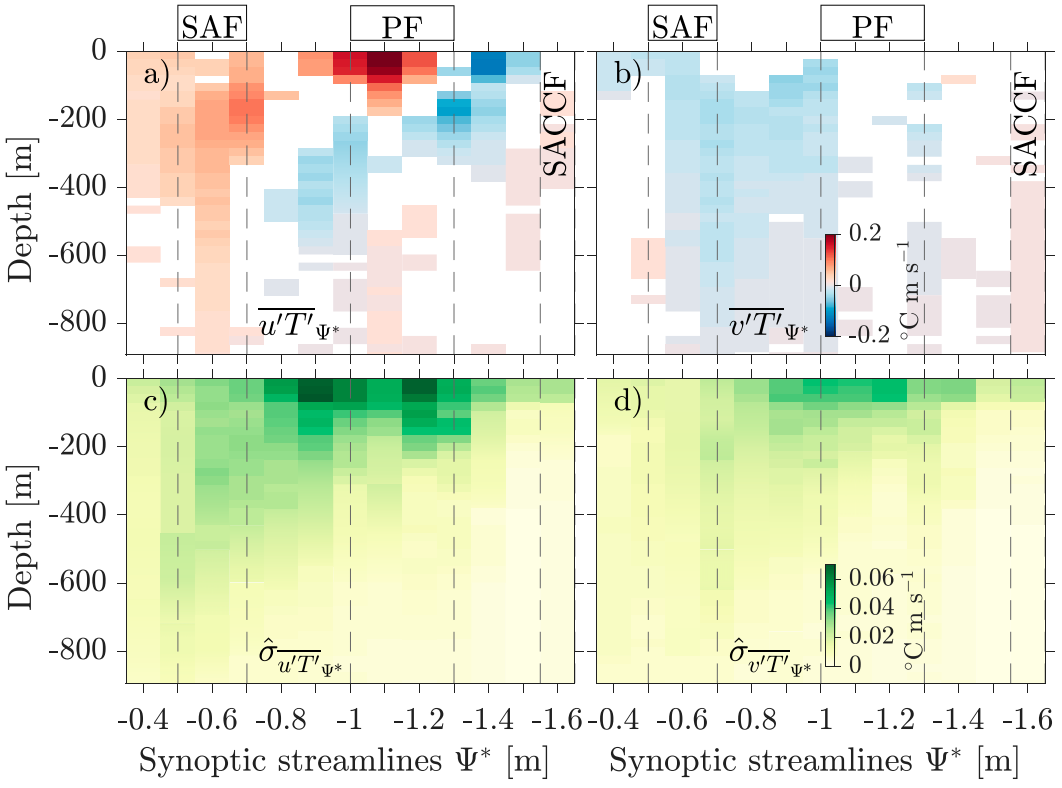

FIG. 5. (a) Along-stream $\overline{u'T'}_{\Psi*}$ and (b) across-stream $\overline{v'T'}_{\Psi*}$ eddy heat flux components, respectively, calculated in a time-varying (synoptic) streamwise coordinate system Ψ^*. Positive along-stream and across-stream values indicate downstream and equatorward heat flux, respectively. Only statistically significant eddy heat flux estimates are shown. (c) Along-stream $\hat{\sigma}_{\overline{u'T'}_{\Psi*}}$ and (d) across-stream $\hat{\sigma}_{\overline{v'T'}_{\Psi*}}$ standard errors. Eddy heat flux components and their standard errors are plotted at $\Delta\Psi^* = 0.10$ m.

downstream in the PF reaching up to 0.19°C m s^{-1} at the surface, and in the SAF ranging from 0.08 at 150 m to 0.01°C m s^{-1} below 600 m (Fig. 5a). In contrast, upstream heat flux is highest (−0.15°C m s^{-1}) south of the PF only in the upper 400 m and significant in the northern flank of the PF between 200- and 400-m depth. The across-stream eddy heat flux component $\overline{v'T'}_{\Psi*}$ (Fig. 5b) shows a different spatial distribution compared to that calculated with $\overline{\Psi}$ (Fig. 4b). A prominent large area of poleward heat flux is located in the SAF and the PFZ; the maximum poleward flux (−0.05°C m s^{-1}) is in the PFZ between 150- and 250-m depth. Everywhere else the across-stream component is marginally significant to insignificant, except for the equatorward heat flux in the SACCF below 200 m. In contrast to the time-mean streamlines (Figs. 4c,d), the largest errors (≥0.02°C m s^{-1}) for both components are located between the PFZ and within the PF; the standard errors near the surface in the PFZ and PF are the largest for the along-stream eddy heat flux component (Figs. 5c,d). Not surprisingly, these standard error patterns are a consequence of the increase in the area defined by the synoptic streamlines associated with the PFZ (therefore, in the number of individual eddy heat flux vectors falling within it) where individual transects cross through strong meandering or rings that have detached from the ACC fronts (Fig. 2).

Figure 6 shows the depth-integrated eddy heat flux components using both the time-mean and synoptic streamlines. For the time-mean case (Fig. 6 dashed lines), the depth-integrated along-stream component $\mathbf{u}'\overline{T'_{\Psi}}$ is upstream in the SAF (−0.12 ± 0.07 GW m^{-1}) and is significantly downstream at two locations: the largest peak is found on the northern flank of the PF (0.19 ± 0.08 GW m^{-1}), and the second peak is found south of the PF (0.06 ± 0.04 GW m^{-1}). The depth-integrated across-stream component for the time-mean streamlines $\overline{v'T'_{\Psi}}$ shows significant poleward heat flux in the region $-0.85 \geq \overline{\Psi} \geq -1.25$ m reaching −0.20 ± 0.10 GW m^{-1} on the southern flank of the PFZ. The SAF exhibits a marginally significant poleward heat flux, but it is a factor-of-2 smaller than that in the northern flank of the PFZ. South of the PF, the across-stream

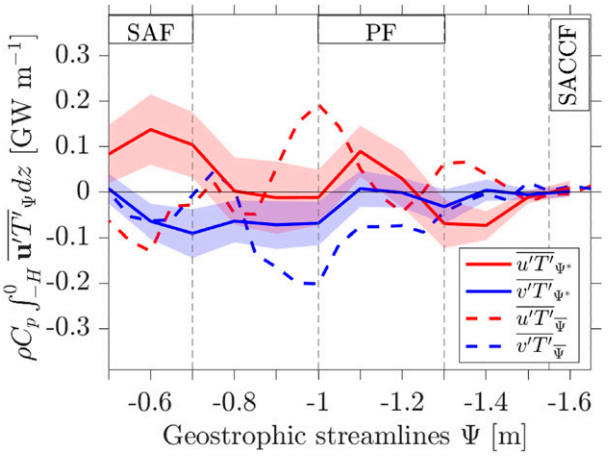

FIG. 6. Depth-integrated along-stream $\overline{u'T'}_{\Psi*}$ (solid red) and across-stream $\overline{v'T'}_{\Psi*}$ (solid blue) eddy heat flux components in a synoptic streamwise coordinate system Ψ^*. Shaded areas show the standard error. Also shown are depth-integrated along-stream $\overline{u'T'}_{\overline{\Psi}}$ (dashed red) and across-stream $\overline{v'T'}_{\overline{\Psi}}$ (dashed blue) components in a time-mean streamwise coordinate system $\overline{\Psi}$. Eddy heat flux components are shown at $\Delta\overline{\Psi} = 0.05$ and $\Delta\Psi^* = 0.10$ m for the time-mean and synoptic streamlines, respectively.

component is statistically insignificant. The across-stream eddy heat flux component for the time-mean case $\overline{v'T'}_{\overline{\Psi}}$ suggests heat convergence in the SAF and south of the PF, and divergence into the PFZ. In contrast, for the synoptic streamwise coordinate system (Fig. 6 solid lines), the depth-integrated along-stream component $\overline{u'T'}_{\Psi*}$ displays two significant downstream heat flux peaks: the largest occurs in the SAF ($0.13 \pm 0.08\,\mathrm{GW\,m^{-1}}$) and a second peak occurs in the PF ($0.08 \pm 0.06\,\mathrm{GW\,m^{-1}}$). Significant upstream flux occurs south of the PF ($-0.07 \pm 0.03\,\mathrm{GW\,m^{-1}}$). For the across-stream component in the synoptic coordinate system $\overline{v'T'}_{\Psi*}$ a single poleward heat flux peak ($-0.10 \pm 0.05\,\mathrm{GW\,m^{-1}}$) is located in the southern flank of the SAF and decreases away from it, such that the poleward heat flux becomes statistically insignificant south of the northern flank of the PF. The largest difference between the two streamwise coordinate systems lies in the amplitudes of the across-stream components in the northern flank the PF; the amplitude of the maximum poleward heat flux for the time-mean streamlines is reduced by 50% when employing the synoptic streamlines. Unlike the depth-integrated $\overline{v'T'}_{\overline{\Psi}}$, the spatial distribution of the depth-integrated $\overline{v'T'}_{\Psi*}$ shows heat convergence south of the SAF.

c. *Seasonal cycle of eddy heat flux and eddy kinetic energy*

We explore the seasonal cycle of the eddy heat flux components in Drake Passage by calculating climatological 3-month mean depth-integrated eddy heat flux components per pair of synoptic streamlines Ψ^*. We used 3-month means to allow more transects, that is, degrees of freedom, for the austral winter months when there are fewer transects. The NB150 ADCP time series was used because it provides 108 concurrent temperature and velocity transects, that is 45 more transects than the OS38 ADCP time series. As described in section 3, both $\mathbf{u}'$ and T' are relative to the time-mean $\overline{\mathbf{u}}$ and $\overline{T}$. No seasonal variation was found for the objectively mapped geostrophic streamlines and velocities (not shown). Each component was rotated, binned and averaged using the synoptic streamwise coordinate system as in method 1 (see appendix A) to yield 108 transects of streamwise-averaged eddy heat flux. For each climatological 3-month window, an average was made of all transects found within the window and assigned to the central month to produce 3-month mean eddy heat flux components per pair of streamlines per depth. These fields were depth integrated, and their 15-yr mean depth-integrated eddy flux was subtracted to produce the 3-month depth-integrated anomalies $\rho C_p \int_{-250}^{0} \overline{\mathbf{u}'T'}^{a}_{\Psi*}\, dz$. We only show statistically significant depth-integrated anomalies (Figs. 7a,b) relative to the mean depth-integrated components (Figs. 7c,d). Both eddy heat flux components show a seasonal cycle. The along-stream heat flux anomalies show upstream heat flux from August to December for almost all geostrophic streamlines; downstream eddy heat flux is ubiquitous from February to June. The anomalies are maximum upstream and downstream in the southern flank of the PFZ for August–September and March–April, respectively (Fig. 7a). For the across-stream component, maximum poleward flux anomalies are found during the austral late autumn and early winter (May–July) reaching $-0.13\,\mathrm{GW\,m^{-1}}$ in the PFZ and northern flank of the PF (Fig. 7b).

The mean seasonal cycle of the depth-averaged 3-month EKE anomalies $\mathrm{EKE}^{a}_{\Psi*} = 1/250 \int_{-250}^{0} 0.5\overline{(u'^2 + v'^2)}^{a}_{\Psi*}$ (using the NB150 ADCP transects paired with an XBT transect) relative to the depth-averaged mean EKE is shown in Fig. 8. In computing the EKE, we employed only those NB150 ADCP transects paired with an XBT transect to better compare with the 3-month eddy heat flux anomalies (Fig. 7). However, the mean EKE calculated from the paired NB150 ADCP–XBT transects ($\overline{\mathrm{EKE}}^{\mathrm{xbt}}_{\Psi*}$; Fig. 8b gray dashed line) is not statistically different relative to that calculated from the full NB150 time series ($\overline{\mathrm{EKE}}_{\Psi*}$; Fig. 8b black solid line). Similar to the across-stream eddy heat flux component, the seasonal cycle of $\mathrm{EKE}^{a}_{\Psi*}$ between the SAF and PF is the largest. However, the maximum $\mathrm{EKE}^{a}_{\Psi*}$ is shifted by 2–3 months with respect to the poleward eddy heat

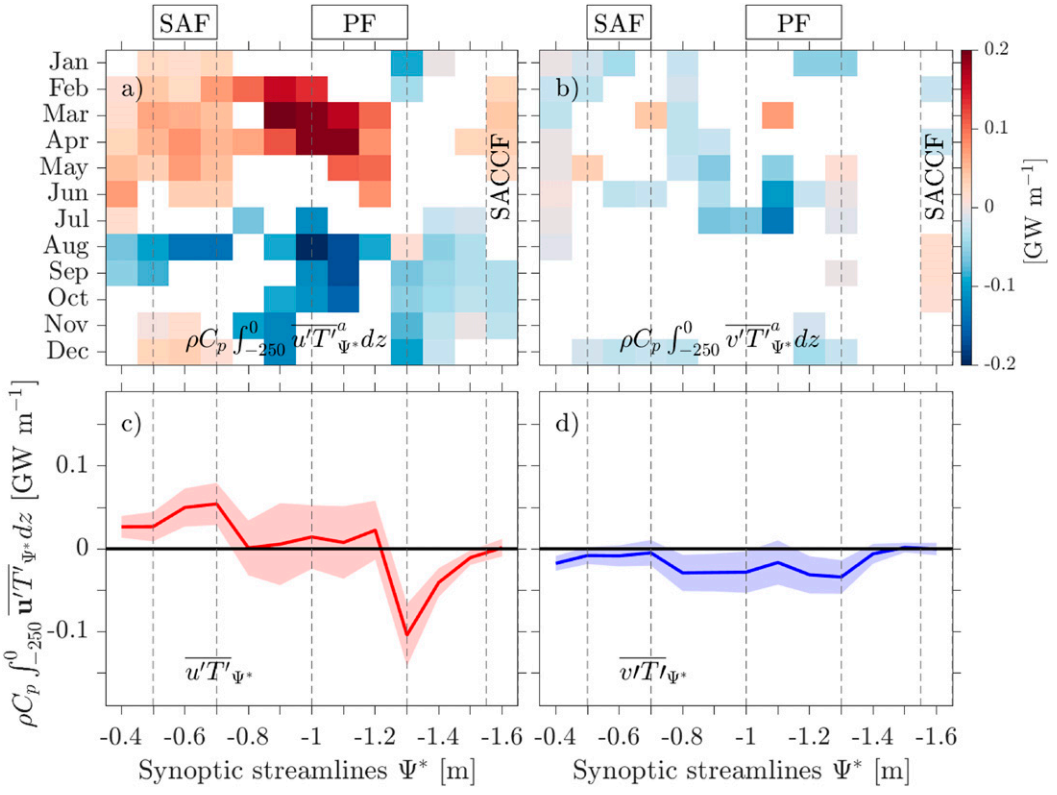

FIG. 7. Three-month mean depth-integrated eddy heat flux anomalies for the (a) along-stream component $\overline{u'T'}^{a}_{\Psi*}$ and (b) across-stream component $\overline{v'T'}^{a}_{\Psi*}$. Three-month anomalies are relative to the 15-yr mean of the (c) along-stream $\overline{u'T'}_{\Psi*}$ and (d) across-stream $\overline{v'T'}_{\Psi*}$ component. Positive along-stream and across-stream values indicate downstream and equatorward heat flux, respectively. Only statistically significant anomalies are shown. Shaded areas in (c) and (d) show the standard errors.

flux 3-month anomalies (Fig. 7b). The positive EKE anomalies are maximum ($\sim$0.03 m^2 s^{-2}) during austral spring–summer in the PFZ (Fig. 8a). Anomalies are negative during austral autumn–winter in the PFZ and at the northern flank of the SAF (Fig. 8a). South of the PF, the maximum amplitude of the seasonal cycle of the $\mathrm{EKE}^{a}_{\Psi*}$ is reduced by a factor of 3.

6. Discussion

a. *Comparisons of eddy heat flux estimates between methods*

The along-stream eddy heat flux component shows two significant poleward peaks at the edges of the Polar Front for the time-mean streamlines (Fig. 6); the largest peak is found in the northern flank of the Polar Front whereas the second peak locates in the southern flank. These two peaks stem from the fact that the time-mean streamfunction masks movement of the front such as the bimodal position of the Polar Front inferred by Foppert et al. (2016). The Polar Front alternated between two preferred locations, either north or south of 58.5°S, the latitude where their observational array crossed the Shackleton Fracture Zone, spending little time in between. The downstream peaks on each of the Polar Front flanks are merged into a broad, significant downstream heat flux peak centered inside the Polar Front when the synoptic streamlines are employed. This single peak is likely consistent with the synoptic streamlines tracking the shifting position of the Polar Front.

Similar to the along-stream eddy heat flux component, the across-stream component shows two significant poleward peaks in the flanks of the Polar Front for the time-mean streamlines (Fig. 6). These double poleward peaks are consistent with Foppert et al. (2016) noting that both Polar Front locations have the necessary conditions for baroclinic instability. The enhanced poleward eddy heat flux in the northern flank of the Polar Front also corresponds with the northern Polar Front proximity to the Polar Front Zone, a more energetic region influenced by bathymetry and deep eddies (Chereskin et al. 2009) than the southern Polar Front location south of the Shackleton Fracture Zone (Fig. 1).

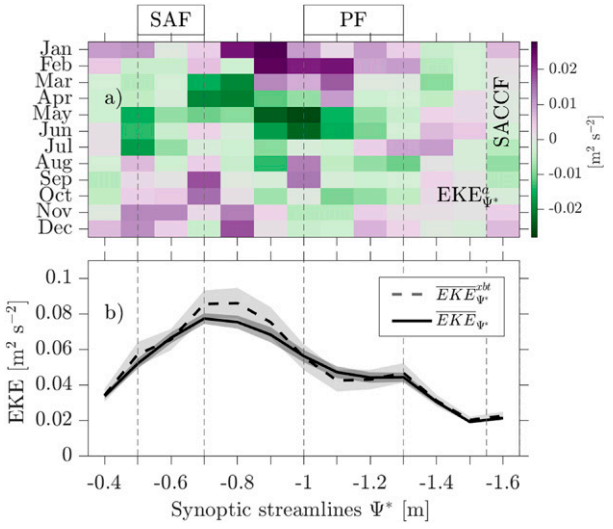

FIG. 8. (a) Three-month mean depth-averaged eddy kinetic energy anomalies $EKE^{a}_{\Psi*}$ calculated relative to the (b) depth-averaged mean eddy kinetic energy determined using the NB150 ADCP transects paired with the XBT transects $\overline{EKE}^{xbt}_{\Psi*}$ (dashed line). The 15-yr mean eddy kinetic energy calculated using all available NB150 ADCP transects $\overline{EKE}_{\Psi*}$ (solid line) is plotted. Shaded areas show the standard error of each mean depth-averaged eddy kinetic energy.

For the synoptic streamwise coordinate system, the across-stream component is poleward everywhere north of the Polar Front. In contrast, the across-stream component relative to the time-mean streamlines shows equatorward heat flux in the northern flank of the Polar Front Zone, and this is most likely due to contamination of the across-stream component by the rotational along-stream component. Downstream of the Shackleton Fracture Zone, the rotational component is associated with regions of equally strong equatorward and poleward eddy heat flux in the Polar Front Zone (Watts et al. 2016) because it is recirculating locally. The poleward eddy heat flux in the Polar Front relative to the time-mean streamlines is reduced by a factor of 2.5 when the synoptic streamlines are employed. As in the Polar Front Zone, this suggests that the across-stream component relative to the time-mean streamlines still has a significant and large contribution from the dynamically irrelevant rotational component that recirculates heat locally and does not contribute to net downgradient eddy heat flux. As a consequence, choosing the time-mean geostrophic streamlines can overestimate the divergent component and give misleading convergence/divergence of heat transport across the ACC streamlines. In contrast to the time-mean streamlines, our results using the synoptic streamlines show heat convergence south of the Subantarctic Front and are consistent with Watts et al. (2016) and Foppert et al. (2017).

The above interpretation assumes that the synoptic streamlines reflect the upper baroclinic structure of the ACC and consequently, any rotation of the total current vector with depth arises from the interaction between the barotropic (depth-independent) flow crossing the baroclinic jet (Watts et al. 2016); that is, the baroclinic current flows parallel to the front while the total current rotates due to the barotropic flow. Veering of the total current near the bottom has been observed in Drake Passage even downstream of the Shackleton Fracture Zone where bottom topography is smoother (Firing et al. 2016). Consequently, eddies transport heat across the ACC front (i.e., down the mean temperature gradient) and release available potential energy from the front when the barotropic component of the flow crosses with optimal phasing. This phasing in which crests and troughs are accompanied by deep highs and lows, respectively, tilted ahead of them downstream is a signature of baroclinic instability (e.g., Vallis 2017; Watts et al. 2016).

b. *Comparisons with previous Southern Ocean eddy heat flux estimates*

To facilitate the comparisons among the different estimates of eddy heat flux in the Southern Ocean, the across-stream eddy heat flux components are multiplied by ρC_p to express the calculated eddy heat flux as an average heat flux per unit area (Fig. 9). The across-stream components per unit area in the upper 900 m, using the time-mean and synoptic streamlines in the Subantarctic Front and Polar Front Zone, agree to within a factor of 3–5 with historical estimates in Drake Passage. However, the eddy heat flux estimate relative to the time-mean streamlines in the southern flank of the Polar Front Zone is maximum and poleward ($\sim -600\,\mathrm{kW\,m^{-2}}$) for the entire Drake Passage area, 2.5 times as large as the poleward heat flux obtained by Lenn et al. (2011) and 8 times as large as that of Ferrari et al. (2014) in the upper 200 m. Moreover, the largest peak found in the southern flank of the Polar Front Zone departs from the divergent eddy heat flux spatial distribution of Watts et al. (2016), which suggests the poleward flux in the Polar Front Zone using the time-mean streamlines is overestimated due to contamination by the rotational component. Lenn et al. (2011) found the largest poleward eddy heat flux occurred in the Southern ACC Front. This disparity with our results reflects the different binning and averaging methodologies and different mean temperatures used to calculate the temperature anomalies in each study. The across-stream eddy heat flux in the Polar Front for the synoptic streamlines is insignificant, implying that the Lenn et al. (2011) estimates might still have a contribution from the rotational

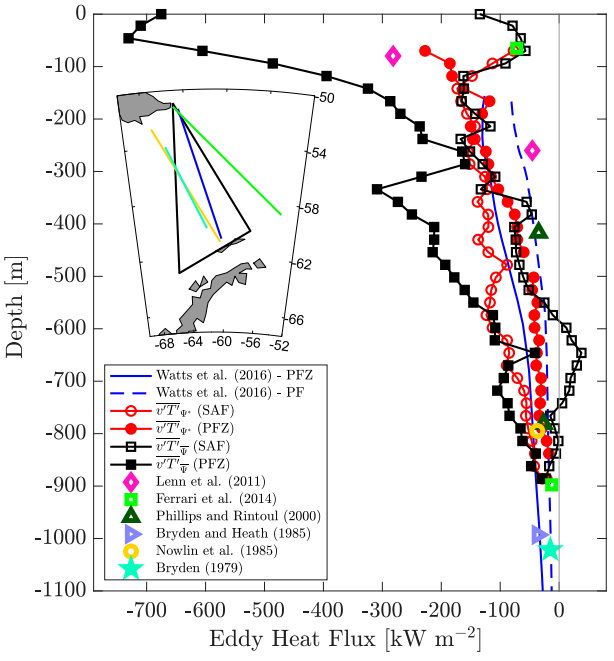

FIG. 9. Historical eddy heat flux estimates from observations in the ACC (symbols). Black squared profiles show this study's across-stream eddy heat flux estimates calculated using the time-mean streamfunction $\overline{v'T'}_{\Psi}$ in the Subantarctic Front (open symbols) and Polar Front Zone (filled symbols). Red circled profiles correspond to this study's across-stream heat flux estimates calculated using the synoptic streamlines $\overline{v'T'}_{\Psi*}$ in the Subantarctic Front (open symbols) and Polar Front Zone (filled symbols). Our estimates were multiplied by ρC_p. Blue solid and dashed profiles show the Watts et al. (2016) divergent meridional eddy heat flux in the Polar Front Zone and Polar Front, respectively. The small inset shows the color-coded locations of historical eddy heat flux estimates in Drake Passage, as referenced in the legend. The black-outlined triangle in the inset shows the area enclosed by the most repeated transects in this study. This figure is adapted from Watts et al. (2016).

component in their across-stream component relative to the time-mean streamlines.

Watts et al. (2016) found significant divergent, meridional eddy heat flux estimates were maximum in the Polar Front Zone. Their poleward heat flux ranges from -130 to $-70\,\mathrm{kW\,m^{-2}}$ between 100 and 300 m and from -50 to $-10\,\mathrm{kW\,m^{-2}}$ between 700 and 900 m. The spatial distribution of the depth-integrated across-stream eddy heat flux component relative to the synoptic streamlines (Fig. 6) shows better agreement with that of Watts et al. (2016) than the across-stream component relative to the mean streamlines. The Watts et al. (2016) estimates are from along their main transect that spans Drake Passage (blue line in the inset, Fig. 9), which is located within our area of study (black triangle in the inset, Fig. 9). Our averaged across-stream flux component per ACC unit length calculated with the synoptic streamlines shows maximum poleward heat flux in the southern flank of the Subantarctic Front ($-0.10 \pm 0.05\,\mathrm{GW\,m^{-1}}$) and decreases toward the south, becoming statistically insignificant at the northern flank of the Polar Front. This distribution agrees with the circumpolarly integrated divergent eddy heat flux distribution found by Foppert et al. (2017) using a power-law fit applied to altimetry SSH standard deviation. Our across-stream estimates are integrated over the upper 900 m while Watts et al. (2016) and Foppert et al. (2017) integrated from 150 to 3500 m. In Watts et al. (2016), one-half of the full-depth divergent eddy heat flux was contained in the upper 1000 m. Assuming that our depth-integrated across-stream component represents half of the full-depth eddy heat transport, we double our value to estimate the total poleward eddy heat transport across the Subantarctic Front as $-0.20\,\mathrm{GW\,m^{-1}}$.

North of the Polar Front, the Drake Passage temperature and velocity transects are located upstream of the Watts et al.'s (2016) observations, close to but still downstream of the Shackleton Fracture Zone where Foppert et al. (2017) obtained their inferred maximum poleward depth-integrated eddy heat flux (from -0.20 to $-0.25\,\mathrm{GW\,m^{-1}}$), matching our extrapolated amplitudes in the south flank of the Subantarctic Front (Fig. 6). Our results and Foppert et al.'s (2017) are consistent with idealized channel numerical studies demonstrating that immediately downstream of a topographic ridge, eddy buoyancy flux is maximum and downgradient, consistent with baroclinic instability processes (e.g., Abernathey and Cessi 2014; Barthel et al. 2017; Youngs et al. 2017). For the synoptic streamlines, the spatial distribution of the mean EKE (Fig. 8b) is similar to that of $\overline{v'T'}_{\Psi*}$, that is, maximum in the northern flank of Polar Front Zone and decreasing away from it (Fig. 6). As discussed by Marshall and Shutts (1981), the divergent, downgradient eddy heat flux is locally balanced by upward vertical eddy heat flux; that is, the release of available potential energy is balanced by conversion to EKE. Assuming that our streamlines are parallel to the temperature contours, the maximum poleward eddy heat flux in the northern flank of the Polar Front Zone collocated with the maximum EKE is consistent with the conversion of potential energy to EKE. However, the EKE in Drake Passage is more spread out within the Polar Front Zone while the divergent eddy heat flux is concentrated in a region immediately downstream of the Shackleton Fracture Zone (Foppert et al. 2017; Foppert 2019). This suggests that other processes such as barotropic instability potentially play a role in setting the EKE distribution in Drake Passage. Both baroclinic and barotropic instability processes are found to coexist in regions where the

ACC encounters abrupt topography (e.g., Barthel et al. 2017; Youngs et al. 2017; Foppert 2019).

c. Seasonality

The 3-month eddy heat flux anomalies are poleward during austral autumn–winter, peaking in July in the Polar Front, but are mainly insignificant over the rest of the year (Fig. 7). These poleward anomalies roughly coincide with the maximum ocean heat loss over Drake Passage during the austral winter (Dong et al. 2007; Stephenson et al. 2012). The northward Ekman heat transport exhibits a seasonal cycle: maximum northward Ekman heat transport during late winter and minimum in summer (Dong et al. 2007). Therefore, our results suggest that stronger-than-average northward Ekman heat transport is partially compensated by poleward eddy heat advection in autumn–winter.

An interesting result stems from the mean EKE and the seasonal cycle of EKE anomalies (Fig. 8). In the northern Drake Passage, the positive EKE anomalies start in September–October in the southern flank of the Subantarctic Front, shifting southward to peak in January–February in the southern flank of the Polar Front Zone. Similarly, the negative EKE anomalies in the same front move southward starting in March–April and are maximum in May–June. Consequently, the mean maximum EKE located in the southern flank of the Subantarctic Front is shifted to the southern flank of the Polar Front Zone from austral spring to summer. Rocha et al. (2016) found no seasonal variability of the kinetic energy wavenumber spectra in the upper 250 m of Drake Passage using a subset of the Drake Passage velocity transects. Because wavenumber spectra show the distribution of velocity variance versus length scale rather than location, the seasonal cycle may not be apparent in spectra computed over all of Drake Passage because the seasonal cycle is not uniformly present in space (as shown in Fig. 8a).

The maximum EKE anomalies in the southern Polar Front Zone (Fig. 8a) are out of phase with respect to the maximum poleward eddy heat flux anomalies found in the northern flank of the Polar Front (Fig. 7b). Elucidating the specific process driving the seasonal variability of the EKE and eddy heat flux anomalies is beyond the scope of the present work. However, three mechanisms are possible candidates. First, we suggest that internal processes such as barotropic and baroclinic instabilities could offer an explanation of the seasonal cycle. Stronger barotropic transfer of mean kinetic energy to EKE during the austral spring–summer could explain the larger EKE amplitude when baroclinic instabilities are absent. Mixed barotropic/baroclinic processes are known to modulate the EKE on seasonal time scales in the Kuroshio region (Yang and San Liang 2018). A second process is the imprint of the surface wind stress on the surface geostrophic mesoscale currents. Renault et al. (2017) made a global analysis of the atmosphere and ocean mesoscale activity and found that in western boundary currents and in the ACC eddy hot spots, mesoscale eddy currents are damped by transferring energy to the atmosphere (i.e., negative wind work). We expect that during the austral winter this energy sink is intensified (more negative wind work than average) as the wind stress variance over the ACC is maximum during the winter. This could explain the minimum $\mathrm{EKE}^{a}_{\Psi*}$ during the austral late autumn and winter in the Polar Front Zone and Polar Front. Last, a third mechanism stems from a larger stratification during the austral summer. This would act to potentially increase the horizontal density gradients near the surface due to the surface heat gain from the atmosphere. Consequently, this shoals the mixed layer and provides an intensification of the eddy velocities by thermal wind balance.

7. Summary and conclusions

In this study, we uniquely exploited the along-track high spatial resolution (first-order baroclinic Rossby radius) of the temperature and velocity transects to estimate the eddy heat flux and EKE relative to the ACC fronts in Drake Passage. The eddy heat flux components were calculated using both the time-mean and a time-varying streamwise coordinate system calculated by adding the altimetry daily maps of sea surface height to the time-mean streamfunction.

We have summarized the main results of the across-stream eddy heat flux component calculated using both streamwise coordinate systems in Fig. 10. The time-mean streamwise coordinate system potentially overestimates the across-stream eddy heat flux component, and therefore also the net heat flux across the ACC in Drake Passage. The depth-integrated across-stream heat flux component using the time-mean streamlines (blue arrows in Fig. 10) is maximum and poleward in the southern flank of the Polar Front Zone ($-0.19 \pm 0.08\,\mathrm{GW\,m^{-1}}$); a second smaller poleward peak is found in the southern Subantarctic Front ($-0.12 \pm 0.07\,\mathrm{GW\,m^{-1}}$). Conversely, the synoptic streamlines show that the maximum poleward flux is located at the southern edge of the Subantarctic Front ($-0.10 \pm 0.05\,\mathrm{GW\,m^{-1}}$) and its amplitude is reduced in the Polar Front Zone becoming statistically insignificant in the Polar Front (red arrows in Fig. 10). We conclude that the time-varying, synoptic streamlines provided the best estimate for the dynamically important divergent eddy heat flux component as they allowed for

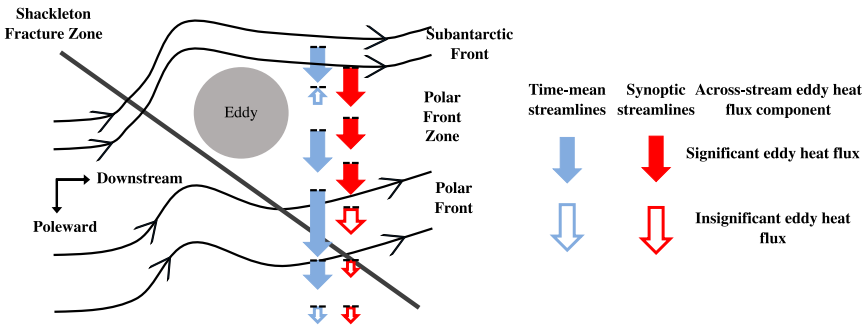

FIG. 10. Plan-view schematic of the eddy heat flux across the ACC fronts in Drake Passage depth-integrated over the upper 900 m (see Fig. 6). Blue and red arrows represent the depth-integrated across-stream eddy heat flux component using the time-mean streamlines $\overline{\Psi}$ and synoptic streamlines Ψ^*, respectively. Filled arrows indicate significant eddy heat flux, whereas nonfilled arrows show insignificant eddy heat flux. Longer arrows indicate a larger across-stream eddy heat flux. Black solid contours show the streamlines of the indicated ACC fronts. Dashed horizontal lines show the location from which the arrow originates. The diagonal line indicates the axis orientation of the Shackleton Fracture Zone. The gray-filled circle indicates where significant eddy activity is found.

the tracking of the ACC streamlines. The time-mean streamlines do not effectively remove the rotational component from the across-stream component. As a consequence, the time-mean streamlines overestimate the conversion from mean to available potential energy in the southern flank of the Polar Front Zone.

Despite the high spatial resolution of the transects, the mean across-stream eddy heat flux south of the Polar Front for both streamwise coordinate systems is insignificant, as also found by Sekma et al. (2013) and Watts et al. (2016) (nonfilled arrows in Fig. 10). This result points to mechanisms other than mesoscale eddies as being responsible for the poleward heat transport in this region in order to balance the ocean heat loss to the atmosphere. Potential candidates are poleward mean heat transport due to the nonequivalent barotropic structure (Peña-Molino et al. 2014) of the ACC and/or mean poleward heat transport due to the temperature changes along the ACC streamlines (Sun and Watts 2002). Alternatively, the insignificant eddy heat flux across the ACC south of the Polar Front could stem from the location of the sampling fan relative to the Shackleton Fracture Zone; the transects lie over a smooth topographic plain, upstream of abrupt topography. Therefore, we would not expect enhanced poleward eddy heat flux due to baroclinic instabilities as found in the northern half of the sampling fan, that is, downstream of the Shackleton Fracture Zone.

The unprecedented 20 years of high-spatial-resolution temperature and velocity transects in the upper 300 m spanning the entire Drake Passage presented an uncommon opportunity to explore the seasonal cycle of the EKE and eddy heat flux components. The eddy heat flux components and EKE for the time-varying streamlines undergo a spatially asymmetric seasonal variability, with a stronger seasonal cycle in the northern Drake Passage streamlines (from the Polar Front toward the north) than in the southern streamlines. The maximum mean EKE located in the northern Polar Front Zone is enhanced during the austral spring and shifts to the southern flank of the Polar Front Zone in summer. In contrast, the across-stream eddy heat flux is maximum poleward during the autumn–winter season in the northern flank of the Polar Front. Mixed barotropic/baroclinic instabilities, wind damping, and stratification are among the potential processes driving the EKE and eddy heat flux seasonal variability. Eddies provide the closure to the Southern Ocean meridional overturning circulation; near the surface, eddies oppose the northward Ekman heat transport whereas deeper in the ocean, eddies are the main mechanism driving upwelling of deep waters along isopycnals. In this context, our results suggest that the eddy-driven upwelling of deep waters has a seasonal component, which is enhanced during austral autumn–winter. Also, we suggest that eddy heat advection plays an important role in the Drake Passage upper-ocean heat budget by partially compensating the stronger-than-average northward Ekman heat transport in autumn–winter. Our results may have implications for the carbon and nutrient cycles in Drake Passage, which have large seasonal and spatial variations (Freeman et al. 2019). More observations and research on these topics are pivotal to fully understand the present and future changes of the Southern Ocean carbon-nutrient cycle and heat budget and to help elucidate the ACC dynamics.

Acknowledgments. We acknowledge the National Science Foundation's Office of Polar Programs Antarctic Division (ANT) and Division of Ocean Sciences (OCE) for support of the Drake Passage time series and this research through Grants ANT-1542902 and OCE-1755529. Author Gutierrez-Villanueva acknowledges support from a University of California Mexus-Conacyt fellowship. XBT temperature data were made available by the Scripps High-Resolution XBT program (http://www-hrx.ucsd.edu). The XBT probes are provided by NOAA's Global Ocean Monitoring and Observing Program through Award NA15OAR4320071. ADCP time series were acquired and processed by the Chereskin Lab at Scripps Institution of Oceanography (http://adcp.ucsd.edu/lmgould/) and can be downloaded from the Joint Archive for Shipboard ADCP (JASADCP) (http://ilikai.soest.hawaii.edu/sadcp/). The SSALTO/DUACS altimeter products were produced and distributed by the Copernicus Marine and Environment Monitoring Service (CMEMS) (http://www.marine.copernicus.eu). The Maximenko et al. (2009) mean dynamic topography for the period 1992–2012 is available online (http://apdrc.soest.hawaii.edu/projects/DOT). We are also grateful to the captain and crew of the ARSV *Laurence M. Gould* and the Antarctic Support Contractor for their excellent technical and logistical support. The authors thank the two anonymous reviewers and the editor whose comments and suggestions greatly improved the paper.

APPENDIX A

Methods for Rotation and Averaging of Eddy Heat Flux Vector in a Time-Varying Streamwise Coordinate System

Here we detail three methods for rotation, binning and averaging of instantaneous eddy heat flux estimates employing a time-varying coordinate system. For the three methods, a general procedure was used for the rotation of individual eddy heat flux estimates for each transect and for the binning of data points (Fig. A1). For each transect, we located velocity and temperature data falling within (i) a specific pair of open streamlines Ψ_j^* and Ψ_{j+1}^* (method 1), where $j = 1, 2, \ldots, M-1$ (M is the total number of unique open streamlines), or (ii) unique intersections between individual transects and open streamlines (methods 2 and 3). For methods 2 and 3, unique intersections were defined where the transect first intersects an open streamline moving in the along-transect direction. Multiple intersections for a specific open streamline were not allowed in methods 2 and 3; that is, once the transect first intersects a streamline Ψ_j^* the along-transect direction is followed until the transect first crosses the next streamline Ψ_{j+1}^*(Figs. A1b,c). Next, individual heat flux estimates were calculated as in the time-mean streamwise coordinate system (the position of each estimate was defined as the position of each temperature profile). The same procedure was used for rotating the eddy heat flux vector into along/across stream components as in the time-mean streamlines, except when data points fell inside closed contours (rings). In that case, the normal vectors found within a pair of open contours or pair of unique intersections that contained closed contours were reinterpolated using an inverse distance weighting method $\hat{\mathbf{n}}' = \sum_{i=1}^{m} \hat{\mathbf{n}} d^{-2} / \sum_{i=1}^{m} d^{-2}$, where $\hat{\mathbf{n}}'$ is the reinterpolated normal vector, m is the number of neighboring data and d is the distance from the m data to the point estimated (Fig. A1). The eddy heat flux vectors were then rotated counterclockwise by $\theta = \theta_{\hat{\mathbf{n}}'} - \pi/2$ where $\theta_{\hat{\mathbf{n}}'}$ is the angle of the reinterpolated normal vector. Last, the resulting eddy heat flux components were binned and averaged first for each pair of streamlines per transect at each depth. Subsequently, each component was averaged to produce mean along-stream $\overline{u'T'}_{\Psi*}$ and across-stream $\overline{v'T'}_{\Psi*}$ eddy heat flux components per streamline at each depth. The following sections list the steps undertaken for binning and averaging the eddy heat flux estimates for each method. In addition, a pair of open streamlines from Fig. A1 is used to illustrate how the rotation was undertaken when data locations were found within closed contours (rings). These examples show how the binning was done for each method and they highlight the key differences among the methods. Last, the depth-integrated components calculated with methods 2 and 3 are shown in appendix B. Method 2 yields larger values for the across-stream component in the SAF relative to methods 1 and 3 by almost a factor of 2. Methods 2 and 3 average over a much larger area covered by a pair of streamlines than does method 1.

a. Method 1: Area between a pair of streamlines

Here we outline the steps for the rotation, binning and averaging of individual eddy heat flux estimates for a pair of open streamlines defined as $\Psi_j^* \geq \Psi^* > \Psi_{j+1}^*$, with $j = 1, 2, \ldots, M-1$ (M is the number of unique streamlines used), $\Psi_{j+1}^* = \Psi_j^* - \Delta\Psi^*$ and $\Psi_{j=1}^*$ is the northernmost streamline (Fig. A1a). For each temperature transect, the following steps were done:

1) Velocity and temperature data were found for each pair of streamlines, and individual eddy heat flux estimates were calculated as undertaken for the time-mean streamlines.
2) Normal vectors were bilinearly interpolated to the individual heat flux positions.

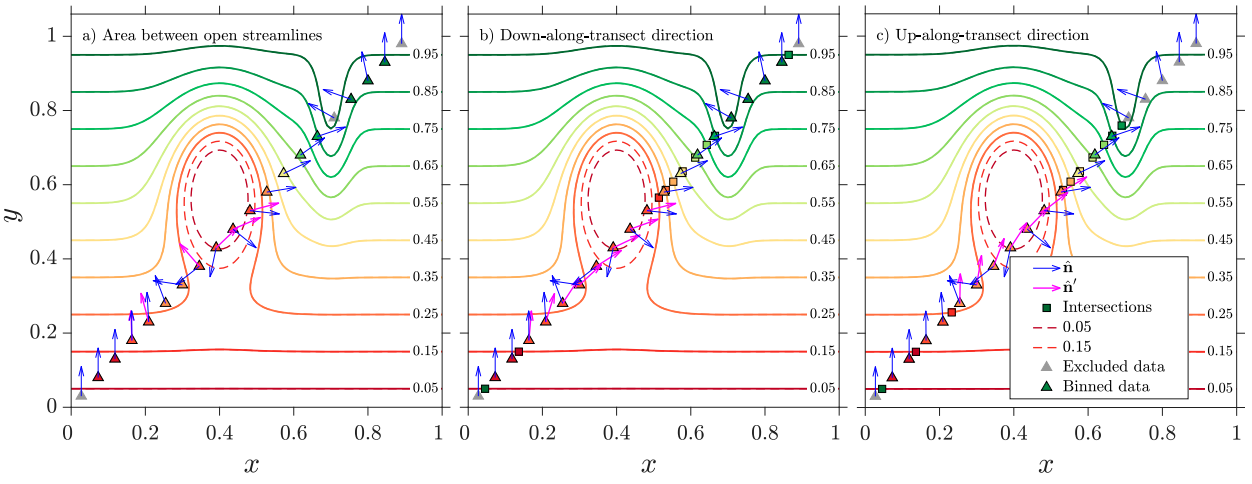

FIG. A1. Idealized schematics illustrating how data points are binned, and the normal vectors $\hat{\mathbf{n}}$ (blue) are calculated using the inverse weighting method $\hat{\mathbf{n}}'$ (magenta) when data points fall inside closed contours (dashed lines) for a specific pair of open streamlines (solid lines) using (a) method 1 (area between open streamlines), (b) method 2 (down-along-transect direction), and (c) method 3 (up-along-transect direction). Data points are colored according to the same pair of open streamlines. Unique intersections are shown with color-coded squares. Data points that fall outside a pair of streamlines (method 1) or a pair of unique intersections (methods 2 and 3) are excluded from the binning and averaging (gray triangles).

3) For the cases when eddy heat flux positions were found within closed contours for a specific pair of open streamlines, all normal vectors enclosed by the pair of open streamlines were reinterpolated using the inverse distance weighting method.
4) Individual estimates were rotated using the angle θ to obtain the along-stream and across-stream components and were averaged per transect per pair of streamlines at each depth.
5) Each component was binned for the pair of streamlines and averaged per transect per pair of streamlines at each depth.
6) The eddy heat flux components were streamwise averaged to produce mean along-stream and across-stream components per pair of streamlines and depth. Standard errors were calculated similarly to the time-mean streamwise coordinate system.

b. *Method 2: Down-along-transect direction*

In contrast to method 1, method 2 uses each transect and the maps of Ψ^* to find unique intersections with open streamlines (Fig. A1b). Moving in the down-along-transect direction, it was determined where each transect first intersected a particular open streamline. The same definitions for Ψ_j^* and Ψ_{j+1}^* were used as in method 1. These steps were followed for the binning, rotation and averaging of the eddy heat flux estimates:

1) Moving in the down-along-transects direction (i.e., starting from the northernmost data position), the first intersection between the transect and the open contour Ψ_j^* and Ψ_{j+1}^* was determined.
2) Velocity and temperature data falling within each pair of intersections were found, and individual eddy heat flux estimates were calculated.
3) Normal vectors were bilinearly interpolated to the eddy heat flux positions.
4) For those positions that were found within closed contours for a specific pair of intersections, every normal vector within the pair of intersections were reinterpolated using the inverse distance weighting method.
5) Individual heat flux estimates were binned and rotated for the pair of streamlines associated with the pair of intersections, to obtain along/across-stream heat flux components.

These steps were repeated for each pair of streamlines per transect and at every depth. Last, the streamwise rotation and averaging were carried out in the same way as in method 1.

c. *Method 3: Up-along-transect direction*

Method 3 followed the same steps used in method 2, but moving in the up-along-transect; that is, unique intersections between open streamlines and each transect were determined by moving from south to north (Fig. A1c). Consequently, $\Psi_{j=1}^*$ is the southernmost streamline and $\Psi_{j+1}^* = \Psi_j^* + \Delta\Psi^*$. The methods described above for methods 1 and 2 were used for interpolation and reinterpolation of the normal vector, as well as for

the rotation, binning and averaging of the eddy heat flux estimates.

d. A case study

As an example, we use the pair of open streamlines $\Psi^* = 0.15$ and $\Psi^* = 0.25$ contoured in Fig. A1a for method 1. Six data points are found inside these open streamlines; one-half of these data points are also located inside closed contours (dashed lines in Fig. A1a). Consequently, the normal vectors $\hat{\mathbf{n}}$ inside the pair of open streamlines were reinterpolated using the normal vector located outside of the pair $\Psi^* = 0.15$ and $\Psi^* = 0.25$. Subsequently, the reinterpolated normal vectors $\hat{\mathbf{n}}'$ (magenta arrows in Fig. A1a) are used to rotate the eddy heat flux estimates into along-stream and across-stream components. These estimates (at locations with magenta arrows in Fig. A1a) are then binned and assigned to the average streamline $\Psi^* = 0.20$.

For method 2 (moving in the down-along-transect direction; Fig. A1b), multiple intersections are found for the northernmost streamline ($\Psi^* = 0.95$); however, only the first intersection ($x = 0.86$) is counted as the method disregards multiple crossings of the same streamline once the first crossing has been found. Moving down-along the transect, the next intersection for $\Psi^* = 0.85$ is found at $x = 0.65$ and the data between this pair of streamlines are rotated and binned in $\Psi^* = 0.90$. No normal vector reinterpolation is required since the transect does not intersect closed streamlines. Moving farther down-along the transect, the first intersection with $\Psi^* = 0.25$ occurs at $x = 0.50$, and we intersect closed contours and $\Psi^* = 0.25$ twice again between $0.20 < x < 0.40$. However, we disregard the duplicate intersections and continue moving down-along the transect until the first intersection with an open $\Psi^* = 0.15$ is found ($x = 0.15$). More data points (eight points with magenta arrows in the area between open streamlines, Fig. A1a) are found between these two streamlines than in method 1. Normal vectors between these two streamlines are reinterpolated, and then their corresponding eddy heat flux estimates rotated and binned for the averaged streamline $\Psi^* = 0.20$.

Last, the normal vector interpolation and reinterpolation and binning using method 3 is illustrated in Fig. A1c. Moving in the up-along-transect direction, the first intersections with $\Psi^* = 0.15$ and $\Psi^* = 0.25$ are found in $0.15 < x < 0.25$. Only two data points are found inside this pair of intersections, less than the 6 data points found using method 1 and the eight points found for method 2 for the same pair of open streamlines (Figs. A1a,b). These two points are binned to $\Psi^* = 0.20$. Continuing along the transect, repeated intersections for $\Psi^* = 0.25$ and closed contours are neglected until the first intersection with $\Psi^* = 0.35$ is located ($x = 0.55$). Data points between the intersections at $\Psi^* = 0.25$ and $\Psi^* = 0.35$ are reinterpolated and binned for $\Psi^* = 0.30$ (magenta arrows in Fig. A1c). In contrast, the northernmost 4 of these 6 data points are binned for $\Psi^* = 0.20$ in methods 1 and 2 (Figs. A1a,b).

In the presence of strong meandering and shifting, method 3 excludes more data points when compared with methods 1 and 2 at the northern and southernmost streamlines (Fig. A1c). In particular, strong meandering is present for the last pair of streamlines $\Psi^* = 0.85$ and $\Psi^* = 0.95$ (for $x > 0.60$). The meandering results in the first intersection between the transect and $\Psi^* = 0.95$ occurring at $x = 0.65$, thus the last five data points are excluded from the binning and averaging.

APPENDIX B

Eddy Heat Flux Estimates for Methods 2 and 3

The depth-integrated eddy heat flux components as a function of Ψ^* using methods 2 and 3 are shown in Fig. B1. The spatial structure of the depth-integrated components is similar for both methods in the southern half of the ACC ($\Psi^* \leq -1.10$ m). The along-stream $\overline{u'T'}_{\Psi^*}$ component shows upstream eddy heat flux south of the PF for both methods. Also, the across-stream component $\overline{v'T'}_{\Psi^*}$ is statistically insignificant south of the PF for both methods, which agrees with the results using the time-mean streamlines and method 1 for the synoptic streamlines (Fig. 6). However, the spatial distribution north of the PF exhibits some discrepancies among methods. The along-stream eddy heat flux component in Method 2 is significantly downstream in the southern flank of the SAF and in the PF (Fig. B1a). In method 3, significant downstream eddy heat flux is only found in the PF (Fig. B1b). Method 2 shows significant maximum poleward eddy heat flux occurs in the SAF with a reduced but still significant amplitude in the PFZ. In contrast, $\overline{v'T'}_{\Psi^*}$ is significant and poleward only in the SAF for method 3. The overall $\overline{v'T'}_{\Psi^*}$ spatial distribution resembles the results from method 1 (Fig. 6); the maximum poleward peak is not statistically different among the three methods. Finally, the depth-integrated along-stream $\overline{u'T'}^{\#}_{\Psi^*}$ and across-stream $\overline{v'T'}^{\#}_{\Psi^*}$ eddy heat flux components calculated using methods 2 and 3, where the $^{\#}$ indicates no reinterpolation of the normal vector when data locations fall within closed contours, are also shown (dashed lines in Fig. B1). It is clear that there is little difference in both components using either method

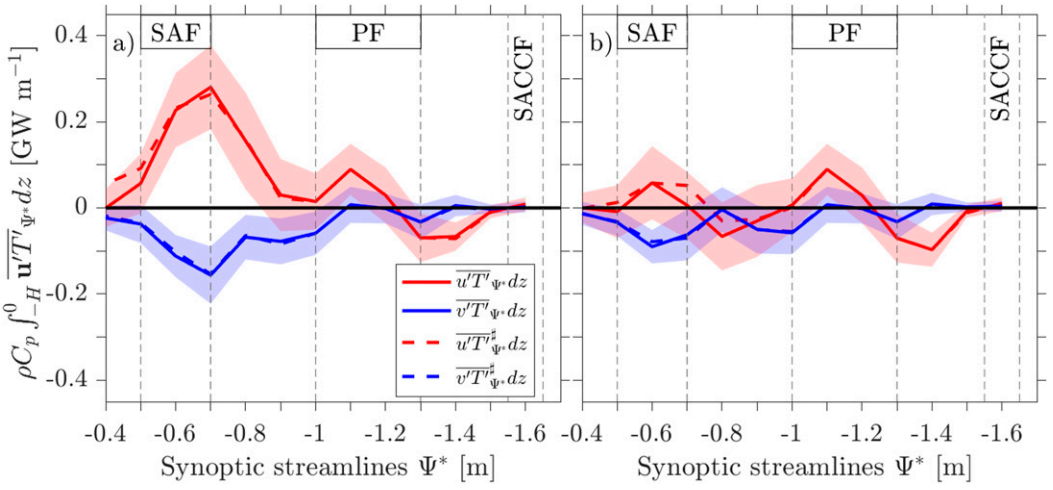

FIG. B1. Depth-integrated eddy heat flux estimates in the upper 886 m as a function of time-varying (synoptic) geostrophic streamfunction Ψ^* calculated using (a) method 2 (moving in the down-along-transect direction) and (b) method 3 (moving in the up-along-transect direction). Solid red and blue lines show the along-stream $\overline{u'T'}_{\Psi*}$ and across-stream $\overline{v'T'}_{\Psi*}$ eddy heat flux components, respectively, when the normal vector is reinterpolated; shaded areas show the standard error. Dashed red and blue lines represent the depth-integrated along-stream $\overline{u'T'}^{\sharp}_{\Psi*}$ and across-stream $\overline{v'T'}^{\sharp}_{\Psi*}$ eddy heat flux components, respectively, calculated without reinterpolating the normal vector when eddy heat flux data locations fell within closed contours.

when the normal vector is reinterpolated or when it is not.

REFERENCES

Abernathey, R., and P. Cessi, 2014: Topographic enhancement of eddy efficiency in baroclinic equilibration. *J. Phys. Oceanogr.*, **44**, 2107–2126, https://doi.org/10.1175/JPO-D-14-0014.1.

Barthel, A., A. McC. Hogg, S. Waterman, and S. Keating, 2017: Jet–topography interactions affect energy pathways to the deep Southern Ocean. *J. Phys. Oceanogr.*, **47**, 1799–1816, https://doi.org/10.1175/JPO-D-16-0220.1.

Bishop, S. P., D. R. Watts, and K. A. Donohue, 2013: Divergent eddy heat fluxes in the Kuroshio extension at 144°–148°E. Part I: Mean structure. *J. Phys. Oceanogr.*, **43**, 1533–1550, https://doi.org/10.1175/JPO-D-12-0221.1.

Bryden, H. L., 1979: Poleward heat flux and conversion of available potential energy in Drake Passage. *J. Mar. Res.*, **37**, 1–22.

Chapman, C., and J.-B. Sallée, 2017: Can we reconstruct mean and eddy fluxes from Argo floats? *Ocean Modell.*, **120**, 83–100, https://doi.org/10.1016/j.ocemod.2017.10.004.

Chelton, D. B., R. A. deSzoeke, M. G. Schlax, K. El Naggar, and N. Siwertz, 1998: Geographical variability of the first baroclinic Rossby radius of deformation. *J. Phys. Oceanogr.*, **28**, 433–460, https://doi.org/10.1175/1520-0485(1998)028<0433:GVOTFB>2.0.CO;2.

Chereskin, T., K. Donohue, D. Watts, K. Tracey, Y. Firing, and A. Cutting, 2009: Strong bottom currents and cyclogenesis in Drake Passage. *Geophys. Res. Lett.*, **36**, L23602, https://doi.org/10.1029/2009GL040940.

Cronin, M., and D. R. Watts, 1996: Eddy–mean flow interaction in the Gulf Stream at 68°W. Part I: Eddy energetics. *J. Phys. Oceanogr.*, **26**, 2107–2131, https://doi.org/10.1175/1520-0485(1996)026<2107:EFIITG>2.0.CO;2.

Dong, S., S. T. Gille, and J. Sprintall, 2007: An assessment of the Southern Ocean mixed layer heat budget. *J. Climate*, **20**, 4425–4442, https://doi.org/10.1175/JCLI4259.1.

Ducet, N., P.-Y. Le Traon, and G. Reverdin, 2000: Global high-resolution mapping of ocean circulation from TOPEX/Poseidon and ERS-1 and-2. *J. Geophys. Res.*, **105**, 19 477–19 498, https://doi.org/10.1029/2000JC900063.

Egbert, G. D., A. F. Bennett, and M. G. Foreman, 1994: TOPEX/Poseidon tides estimated using a global inverse model. *J. Geophys. Res.*, **99**, 24 821–24 852, https://doi.org/10.1029/94JC01894.

Ferrari, R., C. Provost, Y.-H. Park, N. Sennéchael, Z. Koenig, H. Sekma, G. Garric, and R. Bourdallé-Badie, 2014: Heat fluxes across the Antarctic Circumpolar Current in Drake Passage: Mean flow and eddy contributions. *J. Geophys. Res. Oceans*, **119**, 6381–6402, https://doi.org/10.1002/2014JC010201.

Firing, E., J. M. Hummon, and T. K. Chereskin, 2012: Improving the quality and accessibility of current profile measurements in the Southern Ocean. *Oceanography*, **25**, 164–165, https://doi.org/10.5670/oceanog.2012.91.

Firing, Y. L., T. K. Chereskin, and M. R. Mazloff, 2011: Vertical structure and transport of the Antarctic Circumpolar Current in Drake Passage from direct velocity observations. *J. Geophys. Res.*, **116**, C08015, https://doi.org/10.1029/2011JC006999.

——, T. Chereskin, D. Watts, K. Tracey, and C. Provost, 2014: Computation of geostrophic streamfunction, its derivatives, and error estimates from an array of CPIES in Drake Passage. *J. Atmos. Oceanic Technol.*, **31**, 656–680, https://doi.org/10.1175/JTECH-D-13-00142.1.

——, T. K. Chereskin, D. R. Watts, and M. R. Mazloff, 2016: Bottom pressure torque and the vorticity balance from observations in Drake Passage. *J. Geophys. Res. Oceans*, **121**, 4282–4302, https://doi.org/10.1002/2016JC011682.

Foppert, A., 2019: Observed storm track dynamics in Drake Passage. *J. Phys. Oceanogr.*, **49**, 867–884, https://doi.org/10.1175/JPO-D-18-0150.1.

——, K. A. Donohue, and D. R. Watts, 2016: The polar front in Drake Passage: A composite-mean stream-coordinate view. *J. Geophys. Res. Oceans*, **121**, 1771–1788, https://doi.org/10.1002/2015JC011333.

——, ——, ——, and K. L. Tracey, 2017: Eddy heat flux across the Antarctic Circumpolar Current estimated from sea surface height standard deviation. *J. Geophys. Res. Oceans*, **122**, 6947–6964, https://doi.org/10.1002/2017JC012837.

Freeman, N. M., D. R. Munro, J. Sprintall, M. R. Mazloff, S. Purkey, I. Rosso, C. A. DeRanek, and C. Sweeney, 2019: The observed seasonal cycle of macronutrients in Drake Passage: Relationship to fronts and utility as a model metric. *J. Geophys. Res. Oceans*, **124**, 4763–4783, https://doi.org/10.1029/2019JC015052.

Gille, S. T., 2003: Float observations of the Southern Ocean. Part II: Eddy fluxes. *J. Phys. Oceanogr.*, **33**, 1182–1196, https://doi.org/10.1175/1520-0485(2003)033<1182:FOOTSO>2.0.CO;2.

Hanawa, K., P. Rual, R. Bailey, A. Sy, and M. Szabados, 1995: A new depth-time equation for Sippican or TSK T-7, T-6 and T-4 expendable bathythermographs (XBT). *Deep-Sea Res. I*, **42**, 1423–1451, https://doi.org/10.1016/0967-0637(95)97154-Z.

Lenn, Y.-D., and T. K. Chereskin, 2009: Observations of Ekman currents in the Southern Ocean. *J. Phys. Oceanogr.*, **39**, 768–779, https://doi.org/10.1175/2008JPO3943.1.

——, T. Chereskin, J. Sprintall, and E. Firing, 2007: Mean jets, mesoscale variability and eddy momentum fluxes in the surface layer of the Antarctic Circumpolar Current in Drake Passage. *J. Mar. Res.*, **65**, 27–58, https://doi.org/10.1357/002224007780388694.

——, T. K. Chereskin, and J. Sprintall, 2008: Improving estimates of the Antarctic Circumpolar Current streamlines in Drake Passage. *J. Phys. Oceanogr.*, **38**, 1000–1010, https://doi.org/10.1175/2007JPO3834.1.

——, ——, ——, and J. L. McClean, 2011: Near-surface eddy heat and momentum fluxes in the Antarctic Circumpolar Current in Drake Passage. *J. Phys. Oceanogr.*, **41**, 1385–1407, https://doi.org/10.1175/JPO-D-10-05017.1.

Marshall, J., and G. Shutts, 1981: A note on rotational and divergent eddy fluxes. *J. Phys. Oceanogr.*, **11**, 1677–1680, https://doi.org/10.1175/1520-0485(1981)011<1677:ANORAD>2.0.CO;2.

——, and T. Radko, 2003: Residual-mean solutions for the Antarctic Circumpolar Current and its associated overturning circulation. *J. Phys. Oceanogr.*, **33**, 2341–2354, https://doi.org/10.1175/1520-0485(2003)033<2341:RSFTAC>2.0.CO;2.

Maximenko, N., P. Niiler, L. Centurioni, M.-H. Rio, O. Melnichenko, D. Chambers, V. Zlotnicki, and B. Galperin, 2009: Mean dynamic topography of the ocean derived from satellite and drifting buoy data using three different techniques. *J. Atmos. Oceanic Technol.*, **26**, 1910–1919, https://doi.org/10.1175/2009JTECHO672.1.

Meredith, M. P., and Coauthors, 2011: Sustained monitoring of the Southern Ocean at Drake Passage: Past achievements and future priorities. *Rev. Geophys.*, **49**, RG4005, https://doi.org/10.1029/2010RG000348.

Nowlin, W. D., Jr., S. J. Worley, and T. Whitworth III, 1985: Methods for making point estimates of eddy heat flux as applied to the Antarctic Circumpolar Current. *J. Geophys. Res.*, **90**, 3305–3324, https://doi.org/10.1029/JC090iC02p03305.

Orsi, A. H., T. Whitworth III, and W. D. Nowlin Jr., 1995: On the meridional extent and fronts of the Antarctic Circumpolar Current. *Deep-Sea Res. I*, **42**, 641–673, https://doi.org/10.1016/0967-0637(95)00021-W.

Peña-Molino, B., S. Rintoul, and M. Mazloff, 2014: Barotropic and baroclinic contributions to along-stream and across-stream transport in the Antarctic Circumpolar Current. *J. Geophys. Res. Oceans*, **119**, 8011–8028, https://doi.org/10.1002/2014JC010020.

Phillips, H. E., and S. R. Rintoul, 2000: Eddy variability and energetics from direct current measurements in the Antarctic Circumpolar Current south of Australia. *J. Phys. Oceanogr.*, **30**, 3050–3076, https://doi.org/10.1175/1520-0485(2000)030<3050:EVAEFD>2.0.CO;2.

Renault, L., J. C. McWilliams, and S. Masson, 2017: Satellite observations of imprint of oceanic current on wind stress by air-sea coupling. *Sci. Rep.*, **7**, 17747, https://doi.org/10.1038/s41598-017-17939-1.

Rio, M.-H., and F. Hernandez, 2004: A mean dynamic topography computed over the world ocean from altimetry, in situ measurements, and a geoid model. *J. Geophys. Res.*, **109**, C12032, https://doi.org/10.1029/2003JC002226.

Rocha, C. B., T. K. Chereskin, S. T. Gille, and D. Menemenlis, 2016: Mesoscale to submesoscale wavenumber spectra in Drake Passage. *J. Phys. Oceanogr.*, **46**, 601–620, https://doi.org/10.1175/JPO-D-15-0087.1.

Sekma, H., Y.-H. Park, and F. Vivier, 2013: Time-mean flow as the prevailing contribution to the poleward heat flux across the southern flank of the Antarctic Circumpolar Current: A case study in the Fawn Trough, Kerguelen Plateau. *J. Phys. Oceanogr.*, **43**, 583–601, https://doi.org/10.1175/JPO-D-12-0125.1.

Smith, W. H., and D. T. Sandwell, 1997: Global sea floor topography from satellite altimetry and ship depth soundings. *Science*, **277**, 1956–1962, https://doi.org/10.1126/science.277.5334.1956.

Sokolov, S., and S. R. Rintoul, 2009: Circumpolar structure and distribution of the Antarctic Circumpolar Current fronts: 1. Mean circumpolar paths. *J. Geophys. Res.*, **114**, C11018, https://doi.org/10.1029/2008JC005108.

Sprintall, J., 2003: Seasonal to interannual upper-ocean variability in the Drake Passage. *J. Mar. Res.*, **61**, 27–57, https://doi.org/10.1357/002224003321586408.

Stephenson, G. R., S. T. Gille, and J. Sprintall, 2012: Seasonal variability of upper ocean heat content in Drake Passage. *J. Geophys. Res.*, **117**, C04019, https://doi.org/10.1029/2011JC007772.

——, ——, and ——, 2013: Processes controlling upper-ocean heat content in Drake Passage. *J. Geophys. Res.*, **118**, 4409–4423, https://doi.org/10.1002/jgrc.20315.

Sun, C., and D. R. Watts, 2002: Heat flux carried by the Antarctic Circumpolar Current mean flow. *J. Geophys. Res. Oceans*, **107**, 3119, https://doi.org/10.1029/2001JC001187.

Thompson, A. F., and J.-B. Sallée, 2012: Jets and topography: Jet transitions and the impact on transport in the Antarctic Circumpolar Current. *J. Phys. Oceanogr.*, **42**, 956–972, https://doi.org/10.1175/JPO-D-11-0135.1.

——, and A. C. Naveira Garabato, 2014: Equilibration of the Antarctic Circumpolar Current by standing meanders. *J. Phys. Oceanogr.*, **44**, 1811–1828, https://doi.org/10.1175/JPO-D-13-0163.1.

Vallis, G. K., 2017: *Atmospheric and Oceanic Fluid Dynamics*. Cambridge University Press, 773 pp.

Walkden, G. J., K. J. Heywood, and D. P. Stevens, 2008: Eddy heat fluxes from direct current measurements of the Antarctic polar front in shag rocks passage. *Geophys. Res. Lett.*, **35**, L06602, https://doi.org/10.1029/2007GL032767.

Watts, D. R., K. L. Tracey, K. A. Donohue, and T. K. Chereskin, 2016: Estimates of eddy heat flux crossing the Antarctic Circumpolar Current from observations in Drake Passage. *J. Phys. Oceanogr.*, **46**, 2103–2122, https://doi.org/10.1175/JPO-D-16-0029.1.

Yang, Y., and X. San Liang, 2018: On the seasonal eddy variability in the Kuroshio extension. *J. Phys. Oceanogr.*, **48**, 1675–1689, https://doi.org/10.1175/JPO-D-18-0058.1.

Youngs, M. K., A. F. Thompson, A. Lazar, and K. J. Richards, 2017: ACC meanders, energy transfer, and mixed barotropic–baroclinic instability. *J. Phys. Oceanogr.*, **47**, 1291–1305, https://doi.org/10.1175/JPO-D-16-0160.1.